ATLAS NOTE

ATLAS-CONF-2016-085

4th Agust 2016

Search for the Minimal Supersymmetric Standard Model Higgs bosons H/A in the $\tau\tau$ final state in up to 13.3 fb^{-1} of pp collision data at $\sqrt{s} = 13$ TeV with the ATLAS detector

The ATLAS Collaboration

Abstract

A search for neutral Higgs bosons of the Minimal Supersymmetric Standard Model (MSSM) is performed using a data sample from proton–proton collisions at $\sqrt{s} = 13$ TeV recorded by the ATLAS detector at the LHC, corresponding to an integrated luminosity of up to 13.3 fb^{-1}. The heavy resonance is assumed to decay to a $\tau^+\tau^-$ pair with at least one τ lepton decaying hadronically. The search is performed in the mass range of 0.2–1.2 TeV. The data are in good agreement with the background predicted by the Standard Model, hence results are given as upper limits on the production cross section times branching fraction as a function of the Higgs boson mass. The results are interpreted in MSSM benchmark scenarios. The most stringent MSSM parameter space constraints from the search exclude at 95% confidence level $\tan\beta > 9$ for $m_A = 200$ GeV and $\tan\beta > 50$ for $m_A = 1200$ GeV in the $m_h^{\text{mod+}}$ MSSM scenario.

ATLAS-CONF-2016-085
08 August 2016

1. Introduction

The discovery of a scalar particle [1, 2] at the Large Hadron Collider (LHC) [3] has provided important insight into the mechanism of electroweak symmetry breaking. Experimental studies of the new particle [4–8] demonstrate consistency with the Standard Model (SM) Higgs boson [9–14]. However, it remains possible that the discovered particle is part of an extended scalar sector, a scenario that is favoured by a number of theoretical arguments [15, 16].

The Minimal Supersymmetric Standard Model (MSSM) [15, 17, 18] is the simplest extension of the SM that includes supersymmetry. The MSSM requires two Higgs doublets of opposite hypercharge. Assuming that CP symmetry is conserved, this results in one CP-odd (A) and two CP-even (h, H) neutral Higgs bosons and two charged Higgs bosons ($H^{\pm}$). At tree level, the properties of the Higgs sector in the MSSM depend on only two non-SM parameters, which can be chosen to be the mass of the CP-odd Higgs boson, m_A, and the ratio of the vacuum expectation values of the two doublets, $\tan\beta$. Beyond tree level, a number of additional parameters affect the Higgs sector, the choice of which defines various MSSM benchmark scenarios. In some scenarios, such as $m_h^{\text{mod+}}$ [19], the top-squark mixing parameter is chosen such that the mass of the lightest CP-even Higgs boson, m_h, is close to the measured mass of the Higgs boson that was discovered at the LHC. A different approach is employed in the hMSSM scenario [20, 21] in which the measured value of m_h can be used, with certain assumptions, to predict the remaining masses and couplings of the MSSM Higgs bosons without explicit reference to the soft supersymmetry-breaking parameters. The couplings of the MSSM heavy Higgs bosons to down-type fermions are enhanced with respect to the SM for large $\tan\beta$ values, resulting in increased branching fractions to τ leptons and b-quarks,[1] as well as a higher cross section for Higgs boson production in association with b-quarks. This has motivated a variety of searches for a scalar boson in $\tau\tau$ and bb final states at LEP [22], the Tevatron [23–25] and the LHC [26–32].

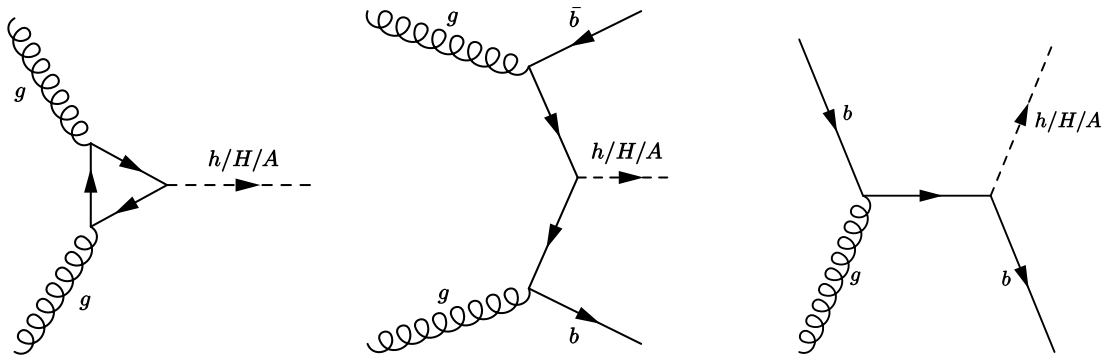

Figure 1: Lowest-order Feynman diagrams for the production of a neutral MSSM Higgs boson via (a) gluon–gluon fusion and b-associated production in the (b) four-flavour and (c) five-flavour schemes of a neutral MSSM Higgs boson.

This paper presents the results of a search for neutral MSSM Higgs bosons in the $\tau\tau$ decay mode using 13.3 fb^{-1} of LHC proton–proton (pp) collision data collected with the ATLAS detector [33] in 2015 and 2016 at a centre-of-mass energy of 13 TeV. From this dataset, 3.2 fb^{-1} were collected in 2015 and 10.1 fb^{-1} in 2016. The search considers the $\tau_{\text{lep}}\tau_{\text{had}}$ and $\tau_{\text{had}}\tau_{\text{had}}$ decay modes, where τ_{lep} represents the

[1] Throughout this paper the inclusion of charge-conjugate decay modes is implied.

decay of a τ lepton to an electron or a muon and neutrinos, while τ_{had} represents the decay to one or more hadrons and a neutrino. The search is performed in the mass range of 0.2–1.2 TeV. Higgs boson production through gluon–gluon fusion and in association with b-quarks is considered (Figure 1), with the latter mode dominating for high $\tan\beta$ values. Hence, both the $\tau_{\text{lep}}\tau_{\text{had}}$ and $\tau_{\text{had}}\tau_{\text{had}}$ channels include b-tag categories to exploit the presence of jets originating from b-quarks in the final state.

2. The ATLAS detector and data sample

The ATLAS detector at the LHC consists of an inner tracking detector with a coverage in pseudorapidity[2] up to $|\eta| = 2.5$, surrounded by a thin superconducting solenoid providing a 2 T axial magnetic field, electromagnetic and hadronic calorimeters extending up to $|\eta| = 4.9$, and a muon spectrometer covering $|\eta| < 2.7$. A new innermost layer was added to the pixel tracking detector after the end of the first run of the LHC at a radial distance of 3.3 cm from the beam line [34]. The ATLAS trigger system consists of a hardware-based first level trigger, followed by a software-based high-level trigger (HLT). The integrated luminosity used in this search, considering the data-taking periods of 2015 and part of 2016 in which all relevant detector subsystems were operational, is 13.3 fb^{-1} (13.2 fb^{-1}) for the $\tau_{\text{lep}}\tau_{\text{had}}$ ($\tau_{\text{had}}\tau_{\text{had}}$) channel. The luminosity measurement and its uncertainty are derived following a methodology similar to that detailed in Ref. [35], from a calibration of the luminosity scale using x–y beam-separation scans performed in August 2015 and in May 2016.

3. Monte Carlo simulation

Simulated events are generated for the neutral MSSM Higgs boson produced via gluon–gluon fusion (ggH) and in association with b-quarks (bbH). Events of the ggH process are generated with `POWHEG-BOX v2` [36–38], while `MADGRAPH5_aMC@NLO 2.1.2` [39, 40] is used for bbH process events. The CT10 [41] and CT10nlo_nf4 [42] sets of parton distribution functions (PDFs) are used, respectively. in the gluon–gluon fusion (b-associated production) `PYTHIA 8.210` [43] with the AZNLO [44] (A14 [45]) set of tuned parameters, or "tune", is used for the parton shower, underlying event and hadronization. The production cross sections for the various MSSM scenarios are calculated using `SusHi` [46] for gluon–gluon fusion [47–59] and b-associated production in the five-flavour scheme [60]; b-associated production in the four-flavour scheme is calculated according to Refs. [61, 62]. The final b-associated production cross section is obtained using the method of Ref. [63] to match the four-flavour and five-flavour scheme cross sections. The masses and couplings of the Higgs bosons are computed with `FeynHiggs` [64–68], whereas the branching fraction calculation follows the procedure described in Ref. [69]. In the case of the hMSSM scenario, the procedure described in Ref. [21] is followed for the production cross sections and `HDECAY` [70] is used for the branching fraction calculation.

The simulated background processes consist of the production of Z+jets, W+jets, $t\bar{t}$ pairs, single top quarks and electroweak dibosons ($WW/WZ/ZZ$). These are modelled with several event generators as

[2] ATLAS uses a right-handed coordinate system with its origin at the nominal interaction point (IP) in the centre of the detector and the z-axis along the beam pipe. The x-axis points from the IP to the centre of the LHC ring, and the y-axis points upwards. Cylindrical coordinates (r, ϕ) are used in the transverse plane, ϕ being the azimuthal angle around the beam pipe. The pseudorapidity is defined in terms of the polar angle θ as $\eta = -\ln\tan(\theta/2)$. Angular distance is measured in units of $\Delta R \equiv \sqrt{(\Delta\eta)^2 + (\Delta\phi)^2}$.

described below, while contributions from multi-jet production are estimated with data-driven techniques as described in Section 6.

Simulated samples of Z+jets events for the $\tau_{\text{lep}}\tau_{\text{had}}$ and $\tau_{\text{had}}\tau_{\text{had}}$ channels and W+jets events for the $\tau_{\text{lep}}\tau_{\text{had}}$ channel are produced using POWHEG-BOX v2 interfaced to PYTHIA 8.186 with the AZNLO tune. In this sample, PHOTOS++ v3.52 [71, 72] is used for photon radiation from electroweak vertices and charged leptons. A dedicated W+jets sample binned in p_{T}^{W}, produced with the SHERPA 2.2.0 generator [73], is used in the $\tau_{\text{had}}\tau_{\text{had}}$ channel in order to enhance the number of events with high $m_{\tau\tau}$ invariant mass. For this sample, matrix elements are calculated for up to two partons at next-to-leading order (NLO) and four partons at LO, merged with the SHERPA parton shower model using the ME+PS@NLO prescription [74]. All W/Z+jets samples use the CT10 PDF set and are normalized to the next-to-next-to-leading-order (NNLO) cross sections calculated using FEWZ [75–77].

The POWHEG-BOX v2 program with the CT10 PDF set is used for the generation of $t\bar{t}$ pairs and single top quarks in the Wt- and s-channels. Samples of t-channel single-top-quark events are produced with the POWHEG-BOX v1 generator employing the four-flavour scheme for the NLO matrix element calculations together with the fixed four-flavour scheme PDF set CT10f4; the top-quark decay is simulated with MadSpin [78]. For all samples of top-quark production, the spin correlations are preserved and the parton shower, fragmentation and underlying event are simulated using PYTHIA 6.428 [79] with the CTQ6L1 PDF set and the corresponding Perugia 2012 tune [80]. Photon radiation from charged leptons and electroweak vertices is simulated using PHOTOS++ v3.52. The top-quark mass is set to 172.5 GeV. The $t\bar{t}$ production sample is normalized to the NNLO cross section, including soft-gluon resummation to next-to-next-to-leading-logarithm accuracy (Ref. [81] and references therein). The normalization of the single top quark event samples uses an approximate NNLO calculation from Refs. [82–84].

Finally, diboson processes are simulated using the SHERPA 2.1.1 program with the CT10 PDF. They are calculated for up to one additional parton at NLO, depending on the process, and up to three additional partons at LO. The diboson samples are normalized to their NLO cross sections, as computed by the event generator.

The simulation of b- and c-hadron decays for all samples, excluding those generated with SHERPA, uses EvtGen v1.2.0 [85]. All simulated samples include the effect of multiple proton–proton interactions in the same and neighbouring bunch crossings ("pile-up") by overlaying simulated minimum-bias events on each generated event. These minimum-bias events are generated with PYTHIA 8.186 [79, 86], using the A2 tune [87] and the MSTW2008LO PDF [88]. For each sample, the ATLAS detector response [89] is simulated using the GEANT4 [90] program, with the exception of the MSSM b-associated Higgs boson signal, for which the ATLFAST-II [89, 91] fast simulation framework is used. Finally, the Monte Carlo (MC) samples are processed through the same reconstruction software as the data.

4. Object reconstruction and identification

The primary vertex of each event is chosen as the proton–proton vertex candidate with the highest sum of the squared transverse momenta of all associated tracks. Electron candidates are reconstructed from energy deposits in the electromagnetic calorimeter associated with a charged-particle track measured in the inner detector. The electron candidates are required to pass a "loose" likelihood-based identification selection [92, 93], to have a transverse energy $E_{\text{T}} > 15$ GeV and to be in the fiducial volume of the inner

detector, $|\eta| < 2.47$. The transition region between the barrel and end-cap calorimeters ($1.37 < |\eta| < 1.52$) is excluded.

Muon candidates are reconstructed from track segments in the muon spectrometer, matched with tracks found in the inner detector within $|\eta| < 2.5$. The tracks of the muon candidates are refit using the complete track information from both detector systems and are required to have a transverse momentum $p_{\mathrm{T}} > 15$ GeV. The muon candidates have to pass a "loose" muon identification requirement [94].

Both the electrons and muons are required to pass a p_{T}-dependent isolation selection, which utilizes both calorimetric and tracking information, with an efficiency of 90% (99%) for transverse momentum of $p_{\mathrm{T}} = 25$ (60) GeV. The isolation provides an efficiency that grows as a function of lepton p_{T}, since the background from jets misidentified as leptons becomes less important as the lepton p_{T} increases.

Jets are reconstructed from topological clusters [95] in the calorimeter using the anti-k_t algorithm [96], with a radius parameter value $R = 0.4$. To reduce the effect of pile-up, a jet vertex tagger algorithm is used for jets with $p_{\mathrm{T}} < 60$ GeV and $|\eta| < 2.4$. It employs a multivariate technique based on jet energy, vertexing and tracking variables to determine the likelihood that the jet originates from pile-up [97]. In order to identify jets containing b-hadrons (b-jets), a multivariate algorithm based on the presence of tracks with a large impact parameter with respect to the primary vertex, the presence of displaced secondary vertices and the reconstructed flight paths of b- and c-hadrons associated with the jet is used [98, 99]. Only jets with $p_{\mathrm{T}} > 25$ GeV and $|\eta| < 2.5$ are considered. A working point that corresponds to an average efficiency of 77% (70%) for b-jets in simulated $t\bar{t}$ events is chosen for the $\tau_{\mathrm{lep}}\tau_{\mathrm{had}}$ ($\tau_{\mathrm{had}}\tau_{\mathrm{had}}$) channel. The misidentification rates for c-jets, τ-jets and jets initiated by light quarks or gluons determined in $t\bar{t}$ simulated events are approximately 16%, 5% and 0.7% (8%, 1.8% and 0.26%), respectively for the 77% (70%) efficiency working point.

Hadronic decays of τ leptons are predominantly characterized by the presence of one or three charged particles, accompanied by a neutrino and possibly neutral pions. The reconstruction of the visible decay products, hereafter referred to as $\tau_{\text{had-vis}}$, is seeded by jets with $p_{\mathrm{T}} > 10$ GeV. The $\tau_{\text{had-vis}}$ candidate must have energy deposits in the calorimeters in the range $|\eta| < 2.5$, with the transition region between the barrel and end-cap calorimeters excluded. Additionally, it must have $p_{\mathrm{T}} > 20$ GeV, one or three associated tracks and an electric charge of ± 1. A multivariate Boosted Decision Tree (BDT) identification procedure, based on calorimetric shower shapes and track multiplicity of the $\tau_{\text{had-vis}}$ candidates, is used to reject backgrounds from jets. In this analysis, two $\tau_{\text{had-vis}}$ identification criteria are used: "loose" and "medium" with efficiencies measured in $Z \to \tau\tau$ decays of about 60% (50%) and 55% (40%) for one-track (three-track) $\tau_{\text{had-vis}}$ candidates, respectively [100]. An additional dedicated likelihood-based veto is used to reduce the number of electrons misidentified as $\tau_{\text{had-vis}}$, providing 95% efficiency and a background rejection between 20 and 200, depending on the pseudorapidity of the $\tau_{\text{had-vis}}$ candidate.

Objects that have a geometric overlap are removed according to the following priorities:

- Jets within a $\Delta R = 0.2$ cone around a selected $\tau_{\text{had-vis}}$ are excluded.
- Jets within a $\Delta R = 0.4$ cone around an electron or muon are excluded.
- Any $\tau_{\text{had-vis}}$ within a $\Delta R = 0.2$ cone around an electron or muon is excluded.
- Electrons within a $\Delta R = 0.2$ cone around a muon are excluded.

The magnitude of the missing transverse momentum vector ($|\vec{E}_{\mathrm{T}}^{\mathrm{miss}}|$) is calculated as the modulus of the negative vectorial sum of the $\vec{p}_{\mathrm{T}}$ of all fully reconstructed and calibrated physics objects [101]. This procedure includes a "soft term", which is calculated based on the inner-detector tracks originating from the hard-scattering vertex that are not associated to reconstructed objects.

5. Search channels

5.1. $\tau_{\mathrm{lep}}\tau_{\mathrm{had}}$ channel

Events in the $\tau_{\mathrm{lep}}\tau_{\mathrm{had}}$ channel are recorded using a combination of $E_{\mathrm{T}}^{\mathrm{miss}}$, single-electron and single-muon triggers. The event selection starts from the events that are fired by a collection of $E_{\mathrm{T}}^{\mathrm{miss}}$ triggers. The threshold of these $E_{\mathrm{T}}^{\mathrm{miss}}$ triggers varies according to the data-taking period and is in the range 70–100 GeV. Events selected by these $E_{\mathrm{T}}^{\mathrm{miss}}$ triggers are required to contain a reconstructed electron or muon and to pass a requirement of $E_{\mathrm{T}}^{\mathrm{miss}} > 150$ GeV for the $\tau_e\tau_{\mathrm{had}}$ channel and $|\vec{E}_{\mathrm{T}}^{\mathrm{miss}} + \vec{p}_{\mathrm{T}}(\mu)| > 150$ GeV for the $\tau_\mu\tau_{\mathrm{had}}$ channel, where $p_{\mathrm{T}}(\mu)$ is the muon transverse momentum. This difference in the requirements between the $\tau_e\tau_{\mathrm{had}}$ and the $\tau_\mu\tau_{\mathrm{had}}$ channels is due to the fact that the $E_{\mathrm{T}}^{\mathrm{miss}}$ reconstruction employed at the trigger level uses only calorimeter information and, hence, muons in the events also contribute to the trigger-level $E_{\mathrm{T}}^{\mathrm{miss}}$. The events selected by this procedure constitute the basis selection for the high-$E_{\mathrm{T}}^{\mathrm{miss}}$ category. In this category, the efficiency of $E_{\mathrm{T}}^{\mathrm{miss}}$ triggers for the simulated backgrounds is derived from data. The efficiency is measured in events selected by single-electron and single-muon triggers that contain a $\tau_{\text{had-vis}}$ candidate and pass the same selection criteria as the signal region. Figure 2 shows examples of the $E_{\mathrm{T}}^{\mathrm{miss}}$ trigger efficiency measurement in (a) the $\tau_e\tau_{\mathrm{had}}$ and (b) the $\tau_\mu\tau_{\mathrm{had}}$ channels, using 2016 data and an $E_{\mathrm{T}}^{\mathrm{miss}}$ trigger with a threshold of 90 GeV. The parametric fit function used to model the trigger efficiency is shown as well.

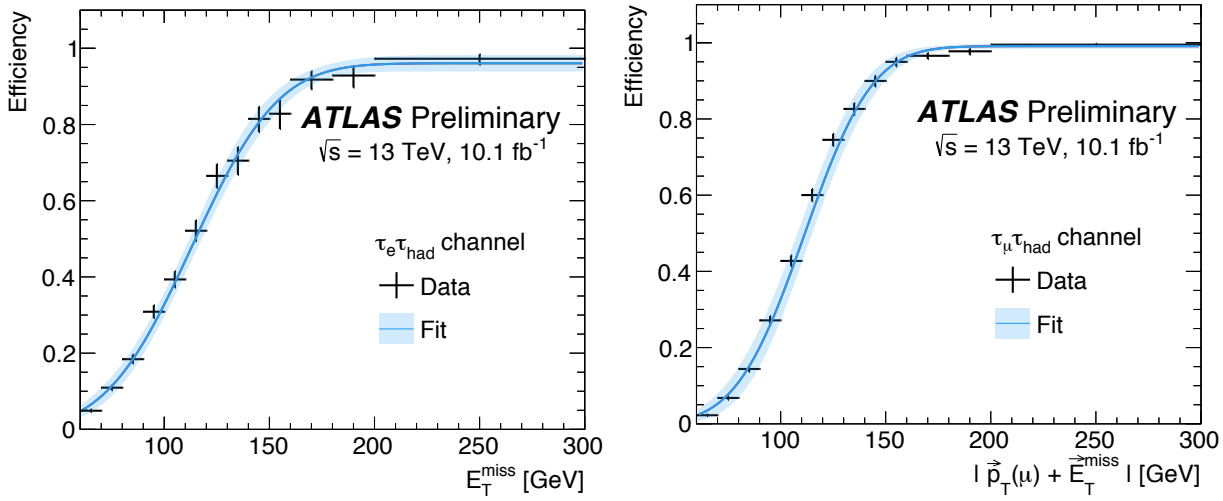

Figure 2: The efficiency of the $E_{\mathrm{T}}^{\mathrm{miss}}$ trigger with a threshold of 90 GeV as measured in data collected in 2016. The data are fit with a sigmoid function and the uncertainties shown are of statistical nature. The fit is shown separately for (a) the $\tau_e\tau_{\mathrm{had}}$ and (b) the $\tau_\mu\tau_{\mathrm{had}}$ channels.

Events with $E_{\mathrm{T}}^{\mathrm{miss}} < 150$ GeV in the $\tau_e\tau_{\mathrm{had}}$ channel ($|\vec{E}_{\mathrm{T}}^{\mathrm{miss}} + \vec{p_{\mathrm{T}}}(\mu)| < 150$ GeV in the $\tau_\mu\tau_{\mathrm{had}}$ channel) are subsequently considered for other selection categories. Events that fire single-electron triggers with p_{T} thresholds of 24 GeV or 26 GeV, 60 GeV, and 120 GeV or 140 GeV, depending on the data-taking period, are selected for the $\tau_e\tau_{\mathrm{had}}$ channel. For the $\tau_\mu\tau_{\mathrm{had}}$ channel, a single-muon trigger with a p_{T} threshold of 50 GeV is used if the muon p_{T} is larger than 55 GeV and a single-muon trigger with a p_{T} threshold of 20 GeV or 26 GeV, depending on the data-taking period, is used otherwise. The triggers impose electron and muon quality requirements which are tighter for the triggers with lower p_{T} thresholds.

Events must have at least one identified $\tau_{\text{had-vis}}$ candidate and either one electron or one muon candidate, which is geometrically matched to the object that triggered the event, in the case where the event is selected by one of the single-lepton triggers. Events with more than one muon or electron fulfilling the criteria described in Section 4 are rejected in order to reduce the backgrounds from $Z/\gamma^* \to \ell\ell$ production where $\ell = e, \mu$. The selected lepton must have a transverse momentum $p_{\mathrm{T}} > 30$ GeV and pass the "medium" identification requirement.

The $\tau_{\text{had-vis}}$ candidate is required to have $p_{\mathrm{T}} > 25$ GeV, to pass the "medium" BDT-based identification requirement and to lie in the range $|\eta| < 2.3$. The latter requirement is motivated by a larger rate of electrons misidentified as $\tau_{\text{had-vis}}$ candidates at higher $|\eta|$ values. If there is more than one $\tau_{\text{had-vis}}$ candidate, the candidate with the highest p_{T} is selected and the others are treated as jets. Finally, the identified lepton and the $\tau_{\text{had-vis}}$ are required to have opposite electric charges.

Subsequently, the following selection requirements are applied:

- $\Delta\phi(\tau_{\text{had-vis}}, \ell) > 2.4$.
- $m_{\mathrm{T}}(\ell, E_{\mathrm{T}}^{\mathrm{miss}}) \equiv \sqrt{2p_{\mathrm{T}}(\ell)E_{\mathrm{T}}^{\mathrm{miss}}[1 - \cos\Delta\phi(\ell, E_{\mathrm{T}}^{\mathrm{miss}})]} < 40$ GeV.
- For the $\tau_e\tau_{\mathrm{had}}$ channel, events are vetoed if the invariant mass of the electron and the visible τ lepton decay products is in the range $80 < m_{\mathrm{vis}}(e, \tau_{\text{had-vis}}) < 110$ GeV.

The requirement on $\Delta\phi(\tau_{\text{had-vis}}, \ell)$ gives an overall reduction of SM backgrounds with little signal loss. The requirement on $m_{\mathrm{T}}(\ell, E_{\mathrm{T}}^{\mathrm{miss}})$ serves to remove events that originate from processes containing a W boson: in signal events the missing transverse momentum is usually in the same direction as the τ_{lep}, resulting in a low value of $m_{\mathrm{T}}(\ell, E_{\mathrm{T}}^{\mathrm{miss}})$. The requirement on $m_{\mathrm{vis}}(e, \tau_{\text{had-vis}})$ reduces the contribution of $Z \to ee$ events where an electron is misidentified as a $\tau_{\text{had-vis}}$ candidate.

The events that are selected by the single-lepton triggers are further categorized to exploit the two different signal production mechanisms according to the presence or not of a jet passing the b-jet identification criterion:

- b-veto category: no b-jets in the event,
- b-tag category: at least one b-jet in the event.

The signal selection efficiency[3] varies in the different $\tau_{\mathrm{lep}}\tau_{\mathrm{had}}$ channel categories. In the b-veto category, it ranges between 6% (2.3%) at $m_A = 200$ GeV and 14% (8%) at $m_A = 1.2$ TeV for the gluon–gluon fusion (b-associated) production mechanism. In the b-tag category, it ranges between 1.4% at $m_A = 200$ GeV and 5% at $m_A = 1.2$ TeV for the b-associated production mechanism. Finally, in the high-$E_{\mathrm{T}}^{\mathrm{miss}}$ category,

[3] The term "signal selection efficiency" refers to the fraction of signal events decaying to $\tau_{\mathrm{lep}}\tau_{\mathrm{had}}$ or $\tau_{\mathrm{had}}\tau_{\mathrm{had}}$ that are subsequently reconstructed within the detector acceptance and pass the selection requirements.

it varies between 0.1% (0.1%) at $m_A = 200$ GeV and 22% (21%) at $m_A = 1.2$ TeV for the gluon–gluon fusion (b-associated) production mechanism.

5.2. $\tau_{\text{had}}\tau_{\text{had}}$ channel

Events in the $\tau_{\text{had}}\tau_{\text{had}}$ channel are selected by a trigger that requires a single $\tau_{\text{had-vis}}$ satisfying the "medium" $\tau_{\text{had-vis}}$ identification criterion and progressively tighter p_{T} requirements as the LHC instantaneous luminosity increased: from $p_{\text{T}} > 80$ GeV to $p_{\text{T}} > 125$ GeV. The leading $\tau_{\text{had-vis}}$ candidate in p_{T} must geometrically match the object that triggered the event. A p_{T} requirement is applied to the leading $\tau_{\text{had-vis}}$ candidate, $p_{\text{T}} > 110$ GeV or $p_{\text{T}} > 140$ GeV, depending on the trigger-level p_{T} threshold. The p_{T} for the sub-leading $\tau_{\text{had-vis}}$ candidate is $p_{\text{T}} > 55$ GeV. Furthermore, the leading (sub-leading) $\tau_{\text{had-vis}}$ candidate has to satisfy the "medium" ("loose") $\tau_{\text{had-vis}}$ identification criterion. Events with electrons or muons fulfilling the loose selection criteria described in Section 4 (with the exception of the isolation requirement) are vetoed to both reduce electroweak background processes and guarantee orthogonality with the $\tau_{\text{lep}}\tau_{\text{had}}$ channel.

The leading and sub-leading $\tau_{\text{had-vis}}$ candidates must have opposite electric charge and have a back-to-back topology in the transverse plane, $\Delta\phi(\tau_{\text{had-vis},1}, \tau_{\text{had-vis},2}) > 2.7$.

The selected $\tau_{\text{had}}\tau_{\text{had}}$ events are categorized in a b-veto and a b-tag category to exploit the two different signal production mechanisms, as discussed for the $\tau_{\text{lep}}\tau_{\text{had}}$ channel in Section 5.1. For the b-tag category, the p_{T} requirement for the sub-leading $\tau_{\text{had-vis}}$ candidate is increased to $p_{\text{T}} > 65$ GeV to improve the modelling of the multi-jet background.

In the b-veto category, the signal selection efficiency varies between 3.2% at $m_A = 300$ GeV and 16% at $m_A = 1.2$ TeV for the gluon–gluon fusion production mode and from 0.9% to 6.7% in the b-tag category for the b-associated production mode.

5.3. Di-τ mass reconstruction

The di-τ mass reconstruction is critical for achieving good separation between signal and background. However, its reconstruction is challenging due to the presence of neutrinos from the τ lepton decays. The mass reconstruction used for both the $\tau_{\text{had}}\tau_{\text{had}}$ and $\tau_{\text{lep}}\tau_{\text{had}}$ channels is the total transverse mass, defined as:

$$m_{\text{T}}^{\text{tot}} = \sqrt{m_{\text{T}}^2(E_{\text{T}}^{\text{miss}}, \tau_1) + m_{\text{T}}^2(E_{\text{T}}^{\text{miss}}, \tau_2) + m_{\text{T}}^2(\tau_1, \tau_2)}, \tag{1}$$

where $m_{\text{T}}(a, b)$ is defined as:

$$m_{\text{T}}(a, b) = \sqrt{2p_{\text{T}}(a)p_{\text{T}}(b)[1 - \cos\Delta\phi(a, b)]} \tag{2}$$

and τ refers to the visible decay products of the τ lepton (ℓ or $\tau_{\text{had-vis}}$). More complex mass reconstruction techniques were investigated, but they were not found to improve the expected sensitivity.

6. Background estimation

The background processes can be categorized according to whether the electron/muon and/or the $\tau_{\text{had-vis}}$ are correctly identified. Backgrounds from processes with correctly identified $\tau_{\text{had-vis}}$, electrons and muons, or where the $\tau_{\text{had-vis}}$ candidate is a misidentified electron/muon in the $\tau_{\text{lep}}\tau_{\text{had}}$ channel, are estimated using simulation, with corrections derived from data. Data-driven techniques are used for processes where the $\tau_{\text{had-vis}}$ or both the lepton and $\tau_{\text{had-vis}}$ are misidentified. The background contributions originating from processes where only the lepton is misidentified are found to be negligible.

6.1. $\tau_{\text{lep}}\tau_{\text{had}}$ background estimation

The main backgrounds in the $\tau_{\text{lep}}\tau_{\text{had}}$ channel arise from processes with a misidentified $\tau_{\text{had-vis}}$, followed by $Z \to \tau\tau$ production in the b-veto category and by $t\bar{t}$ production in the other categories.

Background processes where the τ_{had} candidate, or both the lepton and τ_{had} candidates, arise from misidentified jets are dominated by $t\bar{t}$ (W+jets) and multi-jet processes, for the b-tag (b-veto and high-$E_{\text{T}}^{\text{miss}}$) category. A data-driven "fake-factor" (FF) technique is used to estimate the contribution of these processes to the signal region. The fake factors are derived separately for the 2015 and 2016 datasets by using fake-factor control regions (see Table 1) dominated by a particular background process (Pr), and are defined as:

$$\text{FF(Pr)} = \frac{N(\text{nominal } \tau_{\text{had-vis}} \text{ ID}, \text{Pr})}{N(\text{anti-}\tau_{\text{had-vis}} \text{ ID}, \text{Pr})}, \tag{3}$$

where $N(\text{nominal } \tau_{\text{had-vis}} \text{ ID}, \text{Pr})$ is the number of $\tau_{\text{had-vis}}$ candidates in data satisfying the "medium" $\tau_{\text{had-vis}}$ identification criterion and $N(\text{anti-}\tau_{\text{had-vis}} \text{ ID}, \text{Pr})$ is the number of $\tau_{\text{had-vis}}$ candidates failing this criterion but meeting a looser requirement on the BDT score. The latter requirement defines the "anti-τ_{had}" region, which selects the same kind of objects mimicking $\tau_{\text{had-vis}}$ candidates as those fulfilling the identification criteria. The true τ_{had} contamination in the fake-factor control regions is subtracted based on simulation. In all control regions, the fake factors are parameterized as a function of the transverse momentum and number of tracks of the reconstructed $\tau_{\text{had-vis}}$.

The fake factor for the W+jets and $t\bar{t}$ backgrounds, FF(W+jets/$t\bar{t}$), is determined in control regions that are defined by the same requirements as the signal regions with the exception that the $m_{\text{T}}(\ell, E_{\text{T}}^{\text{miss}})$ requirement is reversed. In particular, the $m_{\text{T}}(\ell, E_{\text{T}}^{\text{miss}})$ requirement becomes $m_{\text{T}}(\ell, E_{\text{T}}^{\text{miss}}) > 70\,(60)$ GeV for the $\tau_e\tau_{\text{had}}$ ($\tau_\mu\tau_{\text{had}}$) channel. The fake factors obtained for the b-tag, b-veto and high-$E_{\text{T}}^{\text{miss}}$ categories by inverting the $m_{\text{T}}(\ell, E_{\text{T}}^{\text{miss}})$ requirement are found to be compatible. Hence, the fake factor derived for the b-veto category is used for all three categories. The purity of the W+jets/$t\bar{t}$ background in this control region is about 95%.

The fake factor for multi-jet (MJ) events, FF(MJ), is measured in control regions that use the same selection criteria as the signal regions with the exception that the isolation requirement on the electron or muon is inverted. The purity for these control regions in MJ events exceeds 99%. Because the high-$E_{\text{T}}^{\text{miss}}$ category fake factor is found to be compatible with the one derived for the b-veto category, the b-veto category fake factor is also used for the high-$E_{\text{T}}^{\text{miss}}$ category to minimize statistical fluctuations.

A correction of the FF(W+jets/$t\bar{t}$) and FF(MJ) fake factors is derived in the W+jets/$t\bar{t}$ and the multi-jet fake factor control regions, respectively. The correction is obtained by comparing the $\Delta(\tau_{\text{had-vis}}, E_{\text{T}}^{\text{miss}})$

$\tau_{\text{lep}}\tau_{\text{had}}$ signal region	$\Delta\phi(\tau_{\text{had-vis}}, \ell) > 2.4$, $m_{\text{T}}(\ell, E_{\text{T}}^{\text{miss}}) < 40$ GeV,
	Veto $80 < m_{e,\tau} < 110$ GeV for $\tau_e\tau_{\text{had}}$,
high-$E_{\text{T}}^{\text{miss}}$ category:	$E_{\text{T}}^{\text{miss}}$ ($\lvert\vec{p_{\text{T}}}(\mu) + \vec{E}_{\text{T}}^{\text{miss}}\rvert$)> 150 GeV for $\tau_e\tau_{\text{had}}$ ($\tau_\mu\tau_{\text{had}}$),
b-tag/b-veto categories:	fail high-$E_{\text{T}}^{\text{miss}}$ category requirements,
	$N_{b\text{-tag}} \geq 1$ (b-tag category), $N_{b\text{-tag}} = 0$ (b-veto category)
b-veto/$t\bar{t}$ fake-factor control region	$m_{\text{T}}(\ell, E_{\text{T}}^{\text{miss}}) > 70$ (60) GeV for $\tau_e\tau_{\text{had}}$ ($\tau_\mu\tau_{\text{had}}$), $N_{b\text{-tag}} = 0$
	different $\tau_{\text{had-vis}}$ identification for the anti-τ_{had} region
b-tag control region	$N_{b\text{-tag}} \geq 1$, $m_{\text{T}}(\ell, E_{\text{T}}^{\text{miss}}) > 100$ GeV
Multi-jet fake-factor control region	invert e, μ isolation requirement,
	$N_{b\text{-tag}} \geq 1$ (b-tag category), $N_{b\text{-tag}} = 0$ (b-veto and high-$E_{\text{T}}^{\text{miss}}$ categories)
	different $\tau_{\text{had-vis}}$ identification for the anti-τ_{had} multi-jet control region
Multi-jet control region for r_{MJ} estimation	$m_{\text{T}}(\ell, E_{\text{T}}^{\text{miss}}) < 30$ GeV, no e, μ isolation requirement,
	no $\tau_{\text{had-vis}}$ passing loose identification,
	$N_{\text{jet}} \geq 1$ and $N_{b\text{-tag}} = 0$ (b-veto category), $N_{\text{jet}} \geq 2$ and $N_{b\text{-tag}} \geq 1$ (b-tag category),
	$N_{\text{jet}} \geq 1$, $N_{b\text{-tag}} = 0$ and $E_{\text{T}}^{\text{miss}}$ ($\lvert\vec{p_{\text{T}}}(\mu) + \vec{E}_{\text{T}}^{\text{miss}}\rvert$)> 150 GeV for
	$\tau_e\tau_{\text{had}}$ ($\tau_\mu\tau_{\text{had}}$) (high-$E_{\text{T}}^{\text{miss}}$ category)

$\tau_{\text{had}}\tau_{\text{had}}$ signal region	$\Delta\phi(\tau_{\text{had-vis},1}, \tau_{\text{had-vis},2}) > 2.7$,
	$N_{b\text{-tag}} \geq 1$ and $p_{\text{T}} > 65$ GeV for the sub-leading $\tau_{\text{had-vis}}$ (b-tag category),
	$N_{b\text{-tag}} = 0$ (b-veto category)
Multi-jet fake-factor control region	pass single-jet trigger,
	leading $\tau_{\text{had-vis}}$ with $p_{\text{T}} > 100$ GeV that fails medium identification,
	no charge requirements and for leading $\tau_{\text{had-vis}}$ $n_{\text{tracks}} \leq 7$ (b-tag category),
	$n_{\text{tracks}} = 1, 3$ (b-veto category), $\frac{p_{\text{T}}^{\tau_{\text{had-vis},2}}}{p_{\text{T}}^{\tau_{\text{had-vis},1}}} > 0.3$
Fake rate control region	pass single-muon trigger, isolated muon with $p_{\text{T}} > 55$ GeV,
	$\tau_{\text{had-vis}}$ with $p_{\text{T}} > 50$ GeV, $\Delta\phi(\mu, \tau_{\text{had-vis}}) > 2.4$,
	$m_{\text{T}}(\mu, E_{\text{T}}^{\text{miss}}) > 40$ GeV
	$N_{b\text{-tag}} \geq 1$ (b-tag category), $N_{b\text{-tag}} = 0$ (b-veto category)
Same-sign validation region	The two $\tau_{\text{had-vis}}$ objects are required
	to have the same electric charge

Table 1: Description of the signal and control regions used in the $\tau_{\text{lep}}\tau_{\text{had}}$ and $\tau_{\text{had}}\tau_{\text{had}}$ channels. For the control regions, only the selection criteria differing from the signal region are enumerated.

distribution of events passing the τ_{had} identification with the prediction obtained from the fake factor measurement. The uncertainty on these corrections of the fake factors amounts to 15%. The shapes and normalization of background contributions in the signal region are then estimated by applying these fake factors to events that pass the anti-τ_{had} region selection but otherwise satisfy all signal region requirements. The fake factors are combined and weighted by the predicted contribution of each background process to the anti-τ_{had} region:

$$\text{FF(comb)} = \text{FF}(W + \text{jets}/t\bar{t}) \times r_{W/t\bar{t}} + \text{FF(MJ)} \times r_{\text{MJ}} \tag{4}$$

where r_{MJ} denotes the fraction of multi-jet events in the anti-τ_{had} region and $r_{W/t\bar{t}} = 1 - r_{\text{MJ}}$. This neglects the differences between the fake factors for W+jets/$t\bar{t}$ and other processes, such as Z production. The parameter r_{MJ} is estimated in two steps using a data-driven method and separately for the b-tag, the b-veto and the high-$E_{\text{T}}^{\text{miss}}$ categories. First, the rates at which jets are misidentified as electrons or muons are measured from the ratio of number of leptons passing and failing the lepton isolation requirement in a region enriched in multi-jet events. This multi-jet control region is defined in Table 1. The predicted

multi-jet rate is then applied to events in the anti-τ_{had} multi-jet control region that also fail the lepton isolation, in order to calculate r_{MJ} as a function of the $\tau_{\text{had-vis}}$ p_{T} separately for the $\tau_e\tau_{\text{had}}$ and $\tau_\mu\tau_{\text{had}}$ channels. When the fake factor is applied to the anti-τ_{had} region events, the contributions of $\tau_{\text{had-vis}}$ from τ_{had} decays and from electrons and muons misidentified as $\tau_{\text{had-vis}}$ candidates are subtracted based on simulation.

Background processes where an electron or a muon is identified as a $\tau_{\text{had-vis}}$ object are modelled based on simulation. Corrections for the misidentification rate of electrons as $\tau_{\text{had-vis}}$ objects are derived from data in a region enriched in $Z(\rightarrow ee)$ events and are applied to simulated events. The main source of such backgrounds is $Z(\rightarrow ee)$+jets events in the $\tau_e\tau_{\text{had}}$ channel, which are reduced using the $m_{\text{vis}}(e,\tau_{\text{had}})$ mass-window veto described in Section 5.1.

The $m_{\text{T}}^{\text{tot}}$ distributions in the $\tau_{\text{lep}}\tau_{\text{had}}$ channel are shown in Figures 3(a) and 3(b) for the b-veto and b-tag control regions, respectively. The latter is identical to the b-tag category definition, except the $m_{\text{T}}(\ell, E_{\text{T}}^{\text{miss}})$ requirement, which is reversed to $m_{\text{T}}(\ell, E_{\text{T}}^{\text{miss}}) > 100$ GeV.

6.2. $\tau_{\text{had}}\tau_{\text{had}}$ background estimation

The dominant background process for the $\tau_{\text{had}}\tau_{\text{had}}$ channel is multi-jet production, the cross section of which is several orders of magnitude higher than that of the signal processes. Despite the large suppression of this background thanks to the event selection, a sizeable contribution of events with two jets misidentified as $\tau_{\text{had-vis}}$ candidates remains. A fake-factor technique is used to normalize and model this background. Fake factors parameterized as a function of p_{T} and the number of tracks of the sub-leading $\tau_{\text{had-vis}}$ object are derived from a control region enriched with multi-jet events, described in Table 1. Requirements on the p_{T} ratio of the two $\tau_{\text{had-vis}}$ objects and the n_{tracks} of the leading $\tau_{\text{had-vis}}$ are imposed to ensure consistency of the backgrounds composition between the signal region and the multi-jet control region. The factors are derived separately for the b-tag and b-veto categories. They are then applied to data events where the leading $\tau_{\text{had-vis}}$ has passed the $\tau_{\text{had-vis}}$ identification requirement in the signal region, while the sub-leading $\tau_{\text{had-vis}}$ candidate fails the loose identification criteria, but has passed a looser requirement on the BDT score. The contributions from non-multi-jet production processes are subtracted based on simulation. In the b-tag category, an additional correction for the fake factors of the one-track $\tau_{\text{had-vis}}$ is measured in the same-sign validation region and applied to both same-sign and opposite-sign regions.

For $t\bar{t}$ and W+jets events, along with other simulated background processes, the probability of a jet being misidentified as a $\tau_{\text{had-vis}}$ is modelled with a "fake rate" technique. The rates of jets being misidentified as a $\tau_{\text{had-vis}}$ object are measured from data as a function of the transverse momentum and number of tracks of the reconstructed $\tau_{\text{had-vis}}$. The fake rate control regions are described in Table 1 and are enriched in $W(\rightarrow \mu\nu)$+jets events for $N_{b\text{-tag}} = 0$ (b-veto category) and $t\bar{t}$ events for $N_{b\text{-tag}} \geq 1$ (b-tag category). The fake rate is then applied to the simulated events as a weight for each of the reconstructed $\tau_{\text{had-vis}}$ candidates that does not geometrically match a true τ lepton. Fake rates derived in the fake rate control region of the b-tag category are used for simulated $t\bar{t}$ and single top quark events, while fake rates obtained in the b-veto control region are applied to the remaining processes.

A same-sign validation region, enriched with events where at least one jet is misidentified as a $\tau_{\text{had-vis}}$ object, is obtained by inverting the opposite-sign requirement of the two $\tau_{\text{had-vis}}$ candidates. Distributions of $m_{\text{T}}^{\text{tot}}$ in the $\tau_{\text{had}}\tau_{\text{had}}$ channel same-sign validation region are shown in Figures 3(c) and 3(d). The good

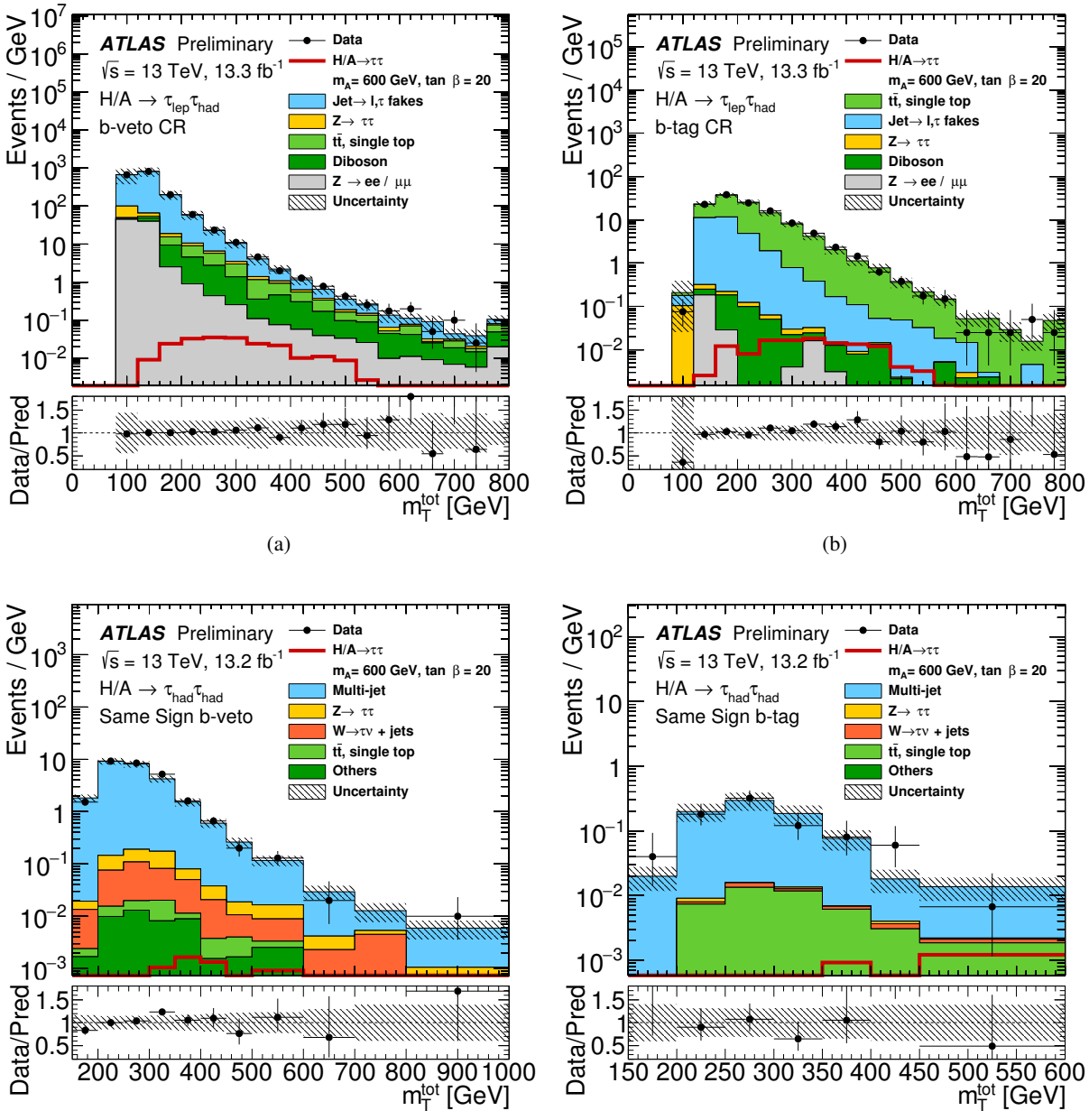

Figure 3: The distributions of $m_{\mathrm{T}}^{\mathrm{tot}}$ in (a) the b-veto control region of the $\tau_{\mathrm{lep}}\tau_{\mathrm{had}}$ channel, (b) the b-tag control region of the $\tau_{\mathrm{lep}}\tau_{\mathrm{had}}$ channel, (c) the b-veto same-sign validation region of the $\tau_{\mathrm{had}}\tau_{\mathrm{had}}$ channel and (d) b-tag same-sign validation region of the $\tau_{\mathrm{had}}\tau_{\mathrm{had}}$ channel. The various control and validation regions are defined in Table 1. The data are compared to the background prediction and a hypothetical MSSM $H/A \rightarrow \tau\tau$ signal ($m_A = 600$ GeV and $\tan\beta = 20$). The statistics of the simulated signal samples are limited in the background-dominated regions. The label "Others" in (c) and (d) refers to contributions from diboson, $Z(\ell\ell)$+jets and $W(\ell\nu)$+jets production. The background uncertainty includes statistical and systematic uncertainties. The bins have a varying size and overflows are included in the last bin of the distributions.

performance of the multi-jet background estimation method is demonstrated by the agreement of the data with the background prediction.

7. Systematic uncertainties

The signal efficiency and the background estimations are affected by uncertainties associated with the detector simulation, the signal modelling and the data-driven background determination.

The integrated luminosity measurement has an uncertainty of 2.1% for the 2015 data and 3.7% for the 2016 data, and it is applied to all simulated event samples. Uncertainties related to the detector are included for the signal and backgrounds that are estimated using simulation. These uncertainties are also taken into account for simulated events that are used in the data-driven background estimations. All instrumental systematic uncertainties arising from the reconstruction, identification and energy scale of $\tau_{\text{had-vis}}$ candidates, electrons, muons, (b-)jets and the soft term of the $E_{\text{T}}^{\text{miss}}$ measurement are considered. The effect of the energy scale uncertainties on the objects is propagated to the $E_{\text{T}}^{\text{miss}}$ determination. The electron, muon, jet and $E_{\text{T}}^{\text{miss}}$ systematic uncertainties described above are found to have a very small impact. In the high-$E_{\text{T}}^{\text{miss}}$ category, the statistical uncertainty of the $E_{\text{T}}^{\text{miss}}$ trigger efficiency measurement is the dominating uncertainty and is taken into account as systematic uncertainty of the measurement. Additionally, the difference observed in simulation between the MC estimated efficiency and the parametric fit result is added to the uncertainty.

Systematic uncertainties resulting from the data-driven background estimations are derived as follows. In the $\tau_{\text{lep}}\tau_{\text{had}}$ channel, the combined fake-factor method includes uncertainties in the W+jets/$t\bar{t}$ fake factors, the multi-jet fake factors, and the r_{MJ} estimation. For the W+jets fake factors, the main uncertainties arise from the dependence on $\Delta\phi(\tau_{\text{had-vis}}, E_{\text{T}}^{\text{miss}})$ and from the difference between the relative contributions of quark- and gluon-initiated jets misidentified as a $\tau_{\text{had-vis}}$ object in the control region and the signal region. The envelope of the fake factor variation as a function of these quantities is used as systematic uncertainty. The fake factor differences between $\tau_e\tau_{\text{had}}$ and $\tau_\mu\tau_{\text{had}}$ channels is also taken into account in the systematic uncertainty. Additionally, the contribution to the uncertainty related to the fake factor difference between signal and control regions is estimated with W+jets simulation events. The fake factor uncertainty is parameterized as a function of the $\tau_{\text{had-vis}}$ p_{T} in the anti-$\tau_{\text{had-vis}}$ region and amounts approximately to 17% for jets misidentified as one-track $\tau_{\text{had-vis}}$ candidates and varies between 16% and 34% for jets misidentified as three-track $\tau_{\text{had-vis}}$ candidates. Uncertainties related to non-W+jets events were studied and have no significant impact on the fake-factor determination. For the multi-jet fake factors and r_{MJ}, the uncertainty is dominated by the limited number of data events in the control region and the subtraction of the remaining non-multi-jet backgrounds using simulation. Typical values of the total uncertainties for r_{MJ} are between 7% and 20% and, for the multi-jet fake factors, between 10% and 20%, depending on the channel and the p_{T} of the $\tau_{\text{had-vis}}$ candidate. In addition, the effect on the background estimate due to the anti-τ_{had} region definition was examined. The loose $\tau_{\text{had-vis}}$ identification requirement used in the definition of this region is varied and the corresponding uncertainty is derived, which is 5% and 1% in the $\tau_e\tau_{\text{had}}$ and $\tau_\mu\tau_{\text{had}}$ channel, respectively. The different amount of multi-jet background is responsible for the uncertainty difference between final states. The resulting uncertainty from all the sources affecting the estimation of backgrounds with jets misidentified as $\tau_{\text{had-vis}}$ is about 30% in the b-tag category and 15% in the other categories.

In the $\tau_{\text{had}}\tau_{\text{had}}$ channel, the uncertainty in the fake factor measurement used for the multi-jet background estimation arises from the statistical uncertainty of the measurement. Other sources of uncertainty include

the definition of the mutli-jet control region and the dependence on the p_{T}, charge and n_{tracks} requirements of the leading $\tau_{\text{had-vis}}$ object. They have been found to have a small impact compared to the statistical component. The fake factor uncertainty varies as a function of the p_{T} of the $\tau_{\text{had-vis}}$. For three-track $\tau_{\text{had-vis}}$ objects, it varies between 14–33% (12–18%) in the b-tag (b-veto) category, while for one-track $\tau_{\text{had-vis}}$ objects, the uncertainty varies between 9–18% (11–14%). The main systematic uncertainty in the estimation of fake rates for jets misidentified as $\tau_{\text{had-vis}}$ arises from the statistical uncertainty of the fake rate measurement and it ranges from 7% to 30% as a function of the p_{T} of the $\tau_{\text{had-vis}}$. The resulting uncertainty on the estimation of backgrounds with jets misidentified as $\tau_{\text{had-vis}}$ is about 15% in both the b-tag and b-veto categories.

Theoretical cross-section uncertainties are taken into account for all backgrounds estimated using simulation. For Z+jets and diboson production, uncertainties of 5% and 6% are used, respectively, combining PDF+α_{S} and scale variation uncertainties in quadrature. For $t\bar{t}$ [81] and single top quark [102, 103] production, a 6% uncertainty is assigned based on scale, PDF and top-quark mass uncertainties. Additional uncertainties related to initial- and final-state radiation modelling, tune and (for $t\bar{t}$ only) the choice of the `hdamp` parameter value in `POWHEG-BOX v2`, which controls the amount of radiation produced by the parton shower, are also taken into account [104]. The uncertainty on the fragmentation model is evaluated by comparing $t\bar{t}$ events generated with `POWHEG-BOX v2` interfaced to either `HERWIG++` [105] or `PYTHIA6`. The `POWHEG+HERWIG++` and `aMC@NLO+HERWIG++` generators are compared to estimate the uncertainty in generating the hard scatter. The variation of acceptance for the $t\bar{t}$ simulated process in the b-tag category arising from these uncertainties is -10% to $+30\%$ (-27% to $+26\%$) in the $\tau_{\text{lep}}\tau_{\text{had}}$ ($\tau_{\text{had}}\tau_{\text{had}}$) channel.

For the signal samples, uncertainties from the factorization and renormalization scale choices are estimated from the effect on the signal acceptance of doubling or halving these factors either coherently or oppositely. Uncertainties due to the initial- and final-state radiation, as well as multiple parton interaction for the signal, are also taken into account. These uncertainties are estimated from the `PYTHIA8` A14 tune [45] for the b-associated production and the AZNLO `PYTHIA8` tune [44] for the gluon–gluon fusion production. The envelope of the variations resulting from the use of the alternative PDFs in the PDF4LHC15_nlo_100 [106] set is used in order to estimate the PDF uncertainty for gluon–gluon fusion production. For the b-associated production uncertainty, a comparison among the following PDFs is employed: NNPDF30_nlo_as_0118_nf_4 [106], CT14nlo_NF4 [42], MSTW2008nlo68cl_nf4 [107] and CT10_nlo_nf4 [41]. Since no statistically significant effect on the shape of the reconstructed mass distribution is observed, each contribution is taken solely as a normalization uncertainty. The total uncertainty for the signal ranges between 15% and 25%.

8. Results

The parameter of interest is the signal strength, μ. It is defined as the ratio of the observed to the predicted value of the cross section times branching fraction, where the prediction is evaluated for a particular MSSM parameter space point assumption. Hence, the value $\mu = 0$ corresponds to the absence of a signal, whereas the value $\mu = 1$ indicates the presence of a signal as predicted by the theoretical model under study. To estimate μ, a likelihood function constructed as the product of Poisson probability terms is used. Signal and background predictions depend on systematic uncertainties, which are parameterized as nuisance parameters and are constrained using Gaussian probability distributions. A binned likelihood function is constructed in bins of the $m_{\mathrm{T}}^{\mathrm{tot}}$ distributions, chosen to ensure sufficient background statistics

in each bin. The asymptotic approximation is used with the test statistic $\tilde{q}_\mu$ [108] to test the compatibility of the data with the assumed signal.

The number of observed $\tau_{\text{lep}}\tau_{\text{had}}$ and $\tau_{\text{had}}\tau_{\text{had}}$ data events in the signal regions, along with the predicted event yields from background and signal processes, are shown in Table 2. The observed event yields are compatible with the expected event yield from SM processes, within uncertainties. The $m_{\text{T}}^{\text{tot}}$ mass distributions are shown in Figure 4. The results from the $\tau_{\text{lep}}\tau_{\text{had}}$ and $\tau_{\text{had}}\tau_{\text{had}}$ channels are combined to improve the sensitivity to H/A boson production.

The fractional contributions of the most important sources of systematic uncertainty to the total uncertainty in the measurement of μ are shown for the MSSM Higgs boson hypothesis $m_A = 600$ GeV, $\tan\beta = 20$ in Table 3.

The data are found to be in good agreement with the predicted background yields and hence the results are given in terms of exclusion limits. These are set using the modified frequentist method known as CL_s [109]. Observed and expected 95% confidence-level (CL) upper limits on the cross section times branching fraction for the production of a single scalar boson H/A decaying to $\tau\tau$, as a function of the mass of the boson $m_{H/A}$, are shown in Figures 5(a) and 5(b). In the case of the $\tau_{\text{had}}\tau_{\text{had}}$ channel, the mass range under study is 300 GeV–1.2 TeV, due to the limited sensitivity for lower mass values. The limits are calculated for both the gluon–gluon fusion and b-associated production modes, using a combination of the $\tau_{\text{lep}}\tau_{\text{had}}$ and $\tau_{\text{had}}\tau_{\text{had}}$ channels and assuming the natural width of the boson to be negligible compared to the experimental resolution (as expected over the probed MSSM parameter space). The lowest excluded cross section times branching fraction values range from $\sigma\times$ BR = 2.0 pb at $m_{H/A} = 200$ GeV to $\sigma\times$ BR = 0.013 pb at $m_{H/A} = 1.2$ TeV for a scalar boson produced via gluon–gluon fusion. Similarly, for the b-associated production mechanism the lowest excluded values range is from $\sigma\times$ BR = 2.1 pb at $m_{H/A} = 200$ GeV to $\sigma\times$ BR = 0.014 pb at $m_{H/A} = 1.2$ TeV.

The observed and expected 95% CL limits on $\tan\beta$ as a function of m_A, for the combination of $\tau_{\text{lep}}\tau_{\text{had}}$ and $\tau_{\text{had}}\tau_{\text{had}}$ channels in the MSSM $m_h^{\text{mod+}}$ and hMSSM scenarios, are shown in Figures 5(c) and 5(d). The expected limit in the $m_h^{\text{mod+}}$ scenario is compared to the expected limits from the individual $\tau_{\text{lep}}\tau_{\text{had}}$ and $\tau_{\text{had}}\tau_{\text{had}}$ channels. The $\tan\beta$ constraints in the hMSSM scenario are stronger than those in the $m_h^{\text{mod+}}$ scenario. This is due to the presence of low-mass neutralinos in the $m_h^{\text{mod+}}$ scenario that reduce the $H/A \to \tau\tau$ branching fraction and which are absent in the hMSSM scenario. In the hMSSM scenario, the most stringent constraints on $\tan\beta$ for the combined search exclude $\tan\beta > 9$ for $m_A = 200$ GeV and $\tan\beta > 42$ for $m_A = 1.2$ TeV at the 95% CL. In this scenario some exclusion sensitivity is observed for low $\tan\beta$ at low m_A values, as well. The expected exclusion limit and bands around $m_A = 350$ GeV reflect the behaviour of the branching ratio $A \to \tau\tau$ close to the $A \to t\bar{t}$ kinematic threshold for low $\tan\beta$, allowing for some exclusion sensitivity in this region. However, when m_A is above the $A \to t\bar{t}$ production threshold, this additional decay mode reduces the sensitivity of the $A \to \tau\tau$ search for low $\tan\beta$. In the MSSM $m_h^{\text{mod+}}$ scenario, the 95% CL upper limits exclude $\tan\beta > 9$ for $m_A = 200$ GeV and $\tan\beta > 50$ for $m_A = 1.2$ TeV.

$\tau_e\tau_{\text{had}}$ channel

	b-tag category			b-veto category			high-$E_{\text{T}}^{\text{miss}}$ category		
$Z \to \tau\tau$+jets	150	±	40	14200	±	900	13	±	2
Jet $\to \ell, \tau_{\text{had-vis}}$ fakes	770	±	260	20000	±	3900	72	±	9
$Z \to \ell\ell$+jets	20	±	4	1370	±	180	-	±	-
$t\bar{t}$ and single top quark	370	±	30	90	±	14	29	±	3
Diboson	3.0	±	0.6	141	±	13	2.6	±	0.6
Total prediction	1320	±	270	35800	±	4000	117	±	11
Data	1304			35841			123		
$m_A = 600$ GeV, $\tan\beta = 20$ ($m_h^{\text{mod+}}$)									
ggH	0.019	±	0.007	1.02	±	0.17	0.32	±	0.06
bbH	4.5	±	0.9	7.2	±	1.5	3.9	±	0.9

$\tau_\mu\tau_{\text{had}}$ channel

	b-tag category			b-veto category			high-$E_{\text{T}}^{\text{miss}}$ category		
$Z \to \tau\tau$+jets	210	±	50	19800	±	1100	91	±	11
Jet $\to \ell, \tau_{\text{had-vis}}$ fakes	960	±	340	18800	±	1900	540	±	60
$Z \to \ell\ell$+jets	10	±	3	1700	±	130	0.22	±	0.08
$t\bar{t}$ and single top quark	350	±	30	85	±	13	187	±	17
Diboson	1.3	±	0.5	190	±	16	14.9	±	2.0
Total prediction	1530	±	350	40600	±	2100	830	±	70
Data	1539			40556			839		
$m_A = 600$ GeV, $\tan\beta = 20$ ($m_h^{\text{mod+}}$)									
ggH	0.010	±	0.004	0.4	±	0.06	1.3	±	0.2
bbH	1.6	±	0.4	3.0	±	0.7	16	±	3

$\tau_{\text{had}}\tau_{\text{had}}$ channel

	b-tag category			b-veto category		
$Z \to \tau\tau$+jets	4.0	±	0.9	340	±	40
Multi-jet	47	±	4	1500	±	60
$W \to \tau\nu$+ jets	1.50	±	0.21	91	±	9
$t\bar{t}$ and single top quark	20	±	6	10	±	6
Others	0.51	±	0.21	14.8	±	2.0
Total prediction	73	±	6	1980	±	40
Data	63			2006		
$m_A = 600$ GeV, $\tan\beta = 20$ ($m_h^{\text{mod+}}$)						
ggH	0.042	±	0.014	3.2	±	0.7
bbH	14	±	4	27	±	8

Table 2: Observed number of events and background predictions in the various categories of the $\tau_e\tau_{\text{had}}$, $\tau_\mu\tau_{\text{had}}$ and $\tau_{\text{had}}\tau_{\text{had}}$ channels. The background predictions and uncertainties are obtained from the statistical procedure discussed in Section 8. In the $\tau_{\text{lep}}\tau_{\text{had}}$ channel, the processes other than "Jet $\to \ell, \tau_{\text{had-vis}}$ fakes" require a true hadronically decaying τ lepton or an electron or muon misidentified as a $\tau_{\text{had-vis}}$. The expected signal yields for the $m_h^{\text{mod+}}$ scenario are shown for $m_A = 600$ GeV and $\tan\beta = 20$ for comparison.

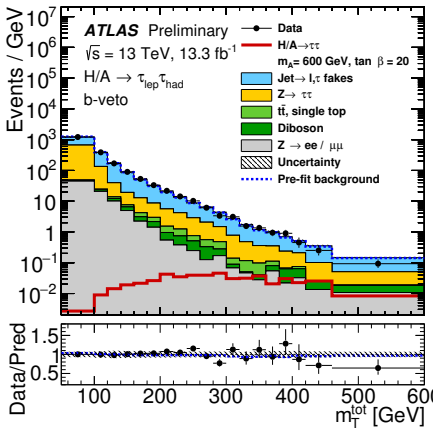

(a) $\tau_{\text{lep}}\tau_{\text{had}}$ b-veto category

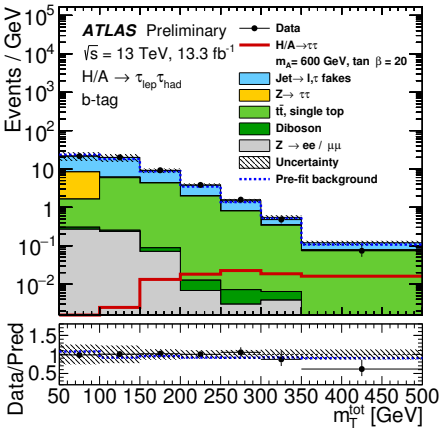

(b) $\tau_{\text{lep}}\tau_{\text{had}}$ b-tag category

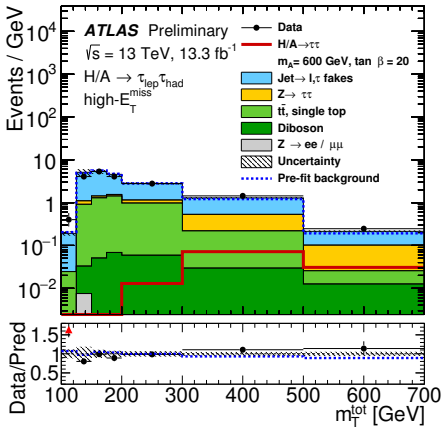

(c) $\tau_{\text{lep}}\tau_{\text{had}}$ high-$E_{\text{T}}^{\text{miss}}$ category

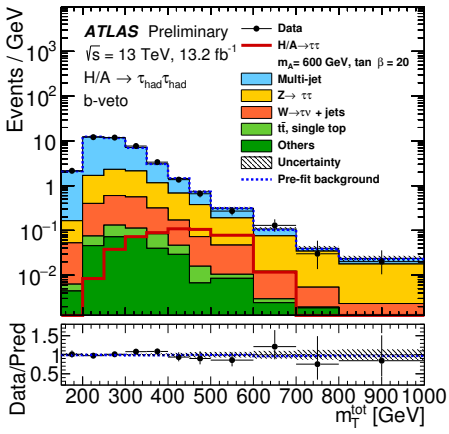

(d) $\tau_{\text{had}}\tau_{\text{had}}$ b-veto category

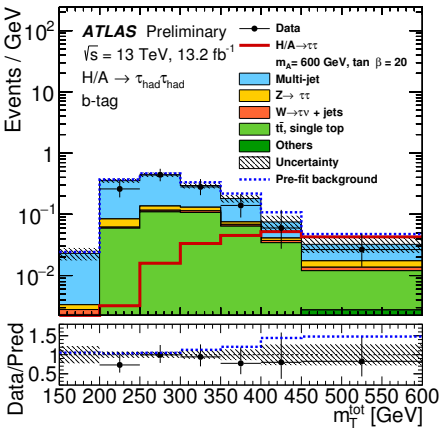

(e) $\tau_{\text{had}}\tau_{\text{had}}$ b-tag category

Figure 4: The distribution of $m_{\text{T}}^{\text{tot}}$ for the (a) b-veto, (b) b-tag, (c) high-$E_{\text{T}}^{\text{miss}}$ categories of the $\tau_{\text{lep}}\tau_{\text{had}}$ and (d) b-veto, (e) b-tag categories of the $\tau_{\text{had}}\tau_{\text{had}}$ channel, The label "Others" in (d) and (e) refers to contributions from diboson, $Z(\ell\ell)$+jets and $W(\ell\nu)$+jets production. The binning displayed is that entering into the statistical fit discussed in Section 8. The predictions and uncertainties for the background processes are obtained from the fit under the hypothesis of no signal. The expectations from signal processes are superimposed. Overflows are included in the last bin of the distributions.

Source of uncertainty	F_- (%)	F_+ (%)
$t\bar{t}$ background parton shower model	−21	+39
$\tau_{\text{had-vis}}$ energy scale, detector modelling	−10	+12
r_{MJ} estimation b-veto region ($\tau_\mu \tau_{\text{had}}$)	− 5	+ 6
r_{MJ} estimation b-veto region ($\tau_e \tau_{\text{had}}$)	− 2.3	+ 3.0
bbH signal cross-section uncertainty	− 3.8	+ 1.6
Multi-jet background ($\tau_{\text{had}} \tau_{\text{had}}$)	− 2.2	+ 2.6
Jet-to-$\tau_{\text{had-vis}}$ fake rate b-veto region ($\tau_{\text{lep}} \tau_{\text{had}}$)	− 1.3	+ 2.9
$\tau_{\text{had-vis}}$ energy scale, in-situ calibration	− 1.4	+ 1.1
r_{MJ} estimation high-$E_{\text{T}}^{\text{miss}}$ region ($\tau_\mu \tau_{\text{had}}$)	− 1.4	+ 1.0
τ trigger (2016)	− 0.5	+ 1.3
Statistics (data and simulation)	−48	+25

Table 3: Fractional impact of the most important sources of systematic uncertainty on the total uncertainty of the signal strength, for the MSSM signal hypothesis of $m_A = 600$ GeV, $\tan\beta = 20$. For each source of uncertainty, $F_\pm = \pm\frac{\sigma^2_{\text{source}}}{\sigma^2_{\text{total}}}$ is defined as the positive (negative) fractional contribution to the signal strength uncertainty.

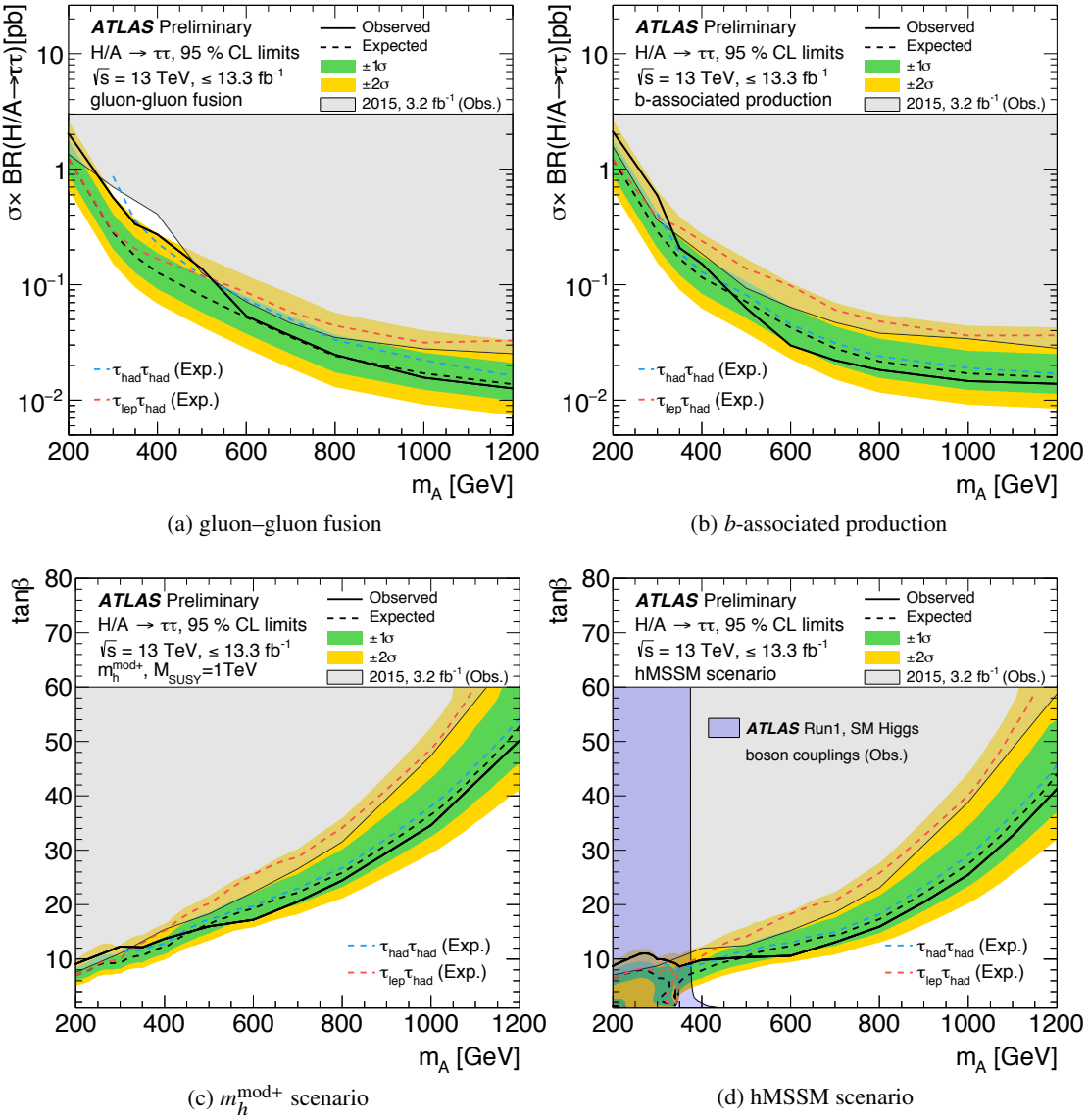

(a) gluon–gluon fusion

(b) b-associated production

(c) $m_h^{\text{mod+}}$ scenario

(d) hMSSM scenario

Figure 5: The observed and expected 95% CL limits on the production cross section times branching fraction of a scalar particle decaying to a $\tau\tau$ pair are shown for the combination of the $\tau_{\text{lep}}\tau_{\text{had}}$ and the $\tau_{\text{had}}\tau_{\text{had}}$ channels. For comparison, the expected limits for the individual channels, $\tau_{\text{lep}}\tau_{\text{had}}$ and $\tau_{\text{had}}\tau_{\text{had}}$, are shown as well. The production mechanism of $H/A \to \tau\tau$ is assumed to be (a) gluon–gluon fusion or (b) b-associated production. The observed and expected 95% CL limits on $\tan\beta$ as a function of m_A are shown in (c) for the MSSM $m_h^{\text{mod+}}$ scenario and (d) for the hMSSM scenario. In the case of the $\tau_{\text{had}}\tau_{\text{had}}$ channel, the mass range under study is 300 GeV–1.2 TeV. In the case of the hMSSM scenario, exclusion limits are set also in the low $\tan\beta$ and $m_A = 200$ GeV region and around the mass value $m_A = 350$ GeV. The exclusion limits are compared to the ATLAS 2015 $H/A \to \tau\tau$ search result of Ref. [31]. For the hMSSM scenario, the exclusion arising from the SM Higgs boson coupling measurements of Ref. [110] is also shown.

9. Conclusions

A search for neutral Higgs bosons of the Minimal Supersymmetric Standard Model decaying to a pair of τ leptons is performed using a data sample from proton–proton collisions at $\sqrt{s} = 13$ TeV recorded by the ATLAS detector at the LHC corresponding to an integrated luminosity of up to 13.3 fb^{-1}. The search finds no indication of an excess over the expected SM background in the channels considered. Hence 95% CL upper limits are set, which provide constraints in the MSSM parameter space. Model-independent upper limits are presented on the production cross section times the $\tau\tau$ branching fraction of a scalar boson versus its mass, in both the gluon–gluon fusion and b-associated production modes. They range from $\sigma\times$ BR = 2.0 (2.1) pb at $m_{H/A} = 200$ GeV to $\sigma\times$ BR = 0.013 (0.014) pb at $m_{H/A} = 1.2$ TeV for a scalar particle produced via gluon–gluon fusion (b-associated production). In the context of the MSSM $m_h^{\text{mod+}}$ scenario, the most stringent 95% CL upper limits on $\tan\beta$ for the combined search are $\tan\beta < 9$ for $m_A = 200$ GeV and $\tan\beta < 50$ for $m_A = 1200$ GeV. This analysis extends the limits set by the previous searches for the mass range $m_A > 350$ GeV.

Appendix

A. Exclusion limits for ggH and bbH cross sections

The cross section limits for scalar particle produced via gluon–gluon fusion or b-associated production are shown in Tables 4–5. These tables present the limits as a function of the scalar particle mass, $m_{H/A}$. The limits are valid under the assumption that the width of the particle is negligible with respect to the $m_{\mathrm{T}}^{\mathrm{tot}}$ mass resolution.

Table 4: Cross section limits for b-associated production. The limit values are in pb.

$\tau\tau$ combination						
m_A [GeV]	observed	expected	$+2\,\sigma$	$+1\,\sigma$	$-1\,\sigma$	$-2\,\sigma$
200	2.1	1.2	2.7	1.8	0.87	0.65
300	0.59	0.29	0.65	0.43	0.21	0.15
350	0.21	0.17	0.39	0.25	0.12	0.090
400	0.15	0.12	0.28	0.18	0.084	0.062
500	0.063	0.071	0.17	0.11	0.051	0.038
600	0.030	0.042	0.10	0.064	0.031	0.023
700	0.022	0.028	0.070	0.044	0.020	0.015
800	0.018	0.022	0.055	0.034	0.016	0.012
1000	0.015	0.017	0.044	0.027	0.012	0.0091
1200	0.014	0.016	0.043	0.025	0.011	0.0085

Table 5: Cross section limits for gluon-fusion. The limit values are in pb.

$\tau\tau$ combination						
m_A [GeV]	observed	expected	$+2\,\sigma$	$+1\,\sigma$	$-1\,\sigma$	$-2\,\sigma$
200	2.0	1.2	2.6	1.8	0.88	0.66
300	0.57	0.28	0.59	0.41	0.20	0.15
350	0.33	0.18	0.37	0.26	0.13	0.094
400	0.27	0.13	0.28	0.19	0.092	0.068
500	0.14	0.080	0.18	0.12	0.058	0.043
600	0.054	0.052	0.12	0.079	0.038	0.028
700	0.036	0.035	0.084	0.054	0.025	0.019
800	0.025	0.024	0.057	0.037	0.017	0.013
1000	0.016	0.017	0.040	0.026	0.012	0.0092
1200	0.013	0.014	0.033	0.021	0.0099	0.0074

B. Two dimensional cross-section limits vs mass and bbH fraction

Tables 6–7 show the two dimensional cross section times branching ratio to $\tau\tau$ limits as a function of the scalar particle mass $m_{H/A}$ and the fraction of the b-associated production cross section, relative to the total cross section, which includes both gluon–gluon fusion and b-associated production, denoted by f_b. The limits are valid under the assumption that the width of the particle is negligible with respect to the $m_{\mathrm{T}}^{\mathrm{tot}}$ mass resolution.

C. Limit plots for other MSSM scenarios

Figure 6 shows the limits on additional MSSM scenarios.

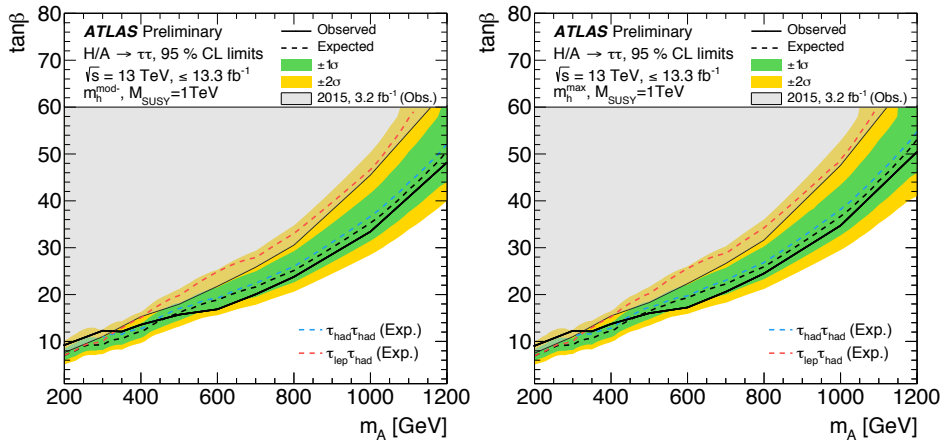

(a) m_h^{max} (b) $m_h^{\mathrm{mod\text{-}}}$

Figure 6: The observed and expected 95% CL upper limits on $\tan\beta$ as a function of m_A for the combination of $\tau_{\mathrm{lep}}\tau_{\mathrm{had}}$ and $\tau_{\mathrm{had}}\tau_{\mathrm{had}}$ channels in the $m_h^{\mathrm{mod\text{-}}}$ and m_h^{max} scenarios with up to 13.3 fb^{-1} of $\sqrt{s}$ = 13 TeV data. These MSSM scenarios are defined in Ref. [19].

D. Limit plots in logarithmic scale for hMSSM scenario

Figure 7 shows the limits on the hMSSM scenario in logarithmic scale. The content is the same as Figure 5.

Table 6: Two dimensional cross-section upper limits on $\sigma\times$ BR as a function of the scalar boson mass $m_{H/A}$ and the b-associated production fraction, f_b, for $m_{H/A} \leq 500$ GeV. The limit values are in pb.

$m_{H/A}$ [GeV]	f_b	observed	expected	$+2\sigma$	$+1\sigma$	-1σ	-2σ
200	1.0	2.1	1.2	2.7	1.8	0.87	0.65
200	0.9	2.2	1.2	2.6	1.8	0.88	0.66
200	0.8	2.2	1.2	2.6	1.8	0.89	0.66
200	0.7	2.2	1.2	2.6	1.8	0.90	0.67
200	0.6	2.2	1.3	2.6	1.8	0.91	0.67
200	0.5	2.2	1.3	2.6	1.8	0.91	0.68
200	0.4	2.2	1.3	2.6	1.8	0.91	0.68
200	0.3	2.1	1.3	2.6	1.8	0.90	0.67
200	0.2	2.1	1.2	2.6	1.8	0.90	0.67
200	0.1	2.1	1.2	2.6	1.8	0.89	0.67
200	0.0	2.0	1.2	2.6	1.8	0.88	0.66
300	1.0	0.59	0.29	0.65	0.43	0.21	0.15
300	0.9	0.62	0.29	0.65	0.44	0.21	0.16
300	0.8	0.64	0.30	0.65	0.44	0.22	0.16
300	0.7	0.65	0.30	0.64	0.44	0.22	0.16
300	0.6	0.66	0.31	0.64	0.44	0.22	0.16
300	0.5	0.66	0.31	0.64	0.44	0.22	0.16
300	0.4	0.65	0.31	0.63	0.44	0.22	0.16
300	0.3	0.64	0.30	0.62	0.44	0.22	0.16
300	0.2	0.63	0.30	0.62	0.43	0.21	0.16
300	0.1	0.60	0.29	0.61	0.42	0.21	0.16
300	0.0	0.57	0.28	0.59	0.41	0.20	0.15
350	1.0	0.21	0.17	0.39	0.25	0.12	0.090
350	0.9	0.24	0.18	0.40	0.26	0.13	0.095
350	0.8	0.26	0.18	0.41	0.27	0.13	0.098
350	0.7	0.29	0.19	0.41	0.28	0.14	0.10
350	0.6	0.31	0.19	0.41	0.28	0.14	0.10
350	0.5	0.33	0.20	0.41	0.28	0.14	0.10
350	0.4	0.34	0.20	0.41	0.28	0.14	0.10
350	0.3	0.34	0.19	0.40	0.28	0.14	0.10
350	0.2	0.35	0.19	0.39	0.27	0.14	0.10
350	0.1	0.34	0.18	0.39	0.27	0.13	0.098
350	0.0	0.33	0.18	0.37	0.26	0.13	0.094
400	1.0	0.15	0.12	0.28	0.18	0.084	0.062
400	0.9	0.17	0.12	0.28	0.18	0.088	0.065
400	0.8	0.20	0.13	0.29	0.19	0.091	0.068
400	0.7	0.22	0.13	0.29	0.20	0.095	0.071
400	0.6	0.24	0.13	0.29	0.20	0.097	0.072
400	0.5	0.25	0.14	0.29	0.20	0.099	0.073
400	0.4	0.26	0.14	0.29	0.20	0.099	0.074
400	0.3	0.27	0.14	0.29	0.20	0.099	0.074
400	0.2	0.27	0.14	0.29	0.20	0.098	0.073
400	0.1	0.27	0.13	0.28	0.19	0.095	0.071
400	0.0	0.27	0.13	0.28	0.19	0.092	0.068
500	1.0	0.063	0.071	0.17	0.11	0.051	0.038
500	0.9	0.069	0.075	0.17	0.11	0.054	0.040
500	0.8	0.076	0.078	0.18	0.12	0.056	0.042
500	0.7	0.084	0.081	0.18	0.12	0.058	0.043
500	0.6	0.092	0.083	0.18	0.12	0.060	0.044
500	0.5	0.10	0.084	0.19	0.12	0.061	0.045
500	0.4	0.11	0.085	0.19	0.13	0.061	0.046
500	0.3	0.12	0.085	0.19	0.13	0.061	0.046
500	0.2	0.13	0.084	0.18	0.12	0.061	0.045
500	0.1	0.13	0.083	0.18	0.12	0.060	0.044
500	0.0	0.14	0.080	0.18	0.12	0.058	0.043

Table 7: Two dimensional cross-section upper limits on $\sigma\times$ BR as a function of the scalar boson mass $m_{H/A}$ and the b-associated production fraction, f_b, for 500 GeV $< m_{H/A} \leq$ 1200 GeV. The limit values are in pb.

$m_{H/A}$ [GeV]	f_b	observed	expected	$+2\sigma$	$+1\sigma$	-1σ	-2σ
600	1.0	0.030	0.042	0.10	0.064	0.031	0.023
600	0.9	0.032	0.045	0.11	0.068	0.032	0.024
600	0.8	0.034	0.047	0.11	0.072	0.034	0.025
600	0.7	0.037	0.049	0.12	0.075	0.035	0.026
600	0.6	0.040	0.051	0.12	0.077	0.037	0.028
600	0.5	0.042	0.053	0.12	0.080	0.038	0.028
600	0.4	0.045	0.054	0.12	0.081	0.039	0.029
600	0.3	0.048	0.055	0.12	0.082	0.039	0.029
600	0.2	0.050	0.055	0.12	0.083	0.039	0.029
600	0.1	0.052	0.054	0.12	0.081	0.039	0.029
600	0.0	0.054	0.052	0.12	0.079	0.038	0.028
700	1.0	0.022	0.028	0.070	0.044	0.020	0.015
700	0.9	0.024	0.029	0.073	0.046	0.021	0.016
700	0.8	0.025	0.031	0.075	0.048	0.022	0.017
700	0.7	0.027	0.032	0.077	0.049	0.023	0.017
700	0.6	0.028	0.033	0.079	0.051	0.024	0.018
700	0.5	0.030	0.034	0.081	0.052	0.025	0.019
700	0.4	0.031	0.035	0.082	0.053	0.026	0.019
700	0.3	0.033	0.036	0.084	0.054	0.026	0.019
700	0.2	0.034	0.036	0.085	0.055	0.026	0.019
700	0.1	0.035	0.036	0.085	0.055	0.026	0.019
700	0.0	0.036	0.035	0.084	0.054	0.025	0.019
800	1.0	0.018	0.022	0.055	0.034	0.016	0.012
800	0.9	0.019	0.022	0.056	0.035	0.016	0.012
800	0.8	0.020	0.023	0.056	0.036	0.017	0.012
800	0.7	0.021	0.024	0.056	0.036	0.017	0.013
800	0.6	0.022	0.024	0.057	0.037	0.017	0.013
800	0.5	0.022	0.025	0.057	0.037	0.018	0.013
800	0.4	0.023	0.025	0.057	0.037	0.018	0.013
800	0.3	0.024	0.025	0.057	0.038	0.018	0.013
800	0.2	0.024	0.025	0.057	0.038	0.018	0.013
800	0.1	0.025	0.025	0.057	0.037	0.018	0.013
800	0.0	0.025	0.024	0.057	0.037	0.017	0.013
1000	1.0	0.015	0.017	0.044	0.027	0.012	0.0091
1000	0.9	0.015	0.017	0.043	0.027	0.012	0.0093
1000	0.8	0.015	0.018	0.043	0.027	0.013	0.0094
1000	0.7	0.015	0.018	0.042	0.027	0.013	0.0094
1000	0.6	0.015	0.018	0.041	0.027	0.013	0.0095
1000	0.5	0.016	0.018	0.041	0.027	0.013	0.0096
1000	0.4	0.016	0.018	0.041	0.027	0.013	0.0096
1000	0.3	0.016	0.018	0.041	0.027	0.013	0.0095
1000	0.2	0.016	0.018	0.040	0.026	0.013	0.0095
1000	0.1	0.016	0.017	0.040	0.026	0.013	0.0093
1000	0.0	0.016	0.017	0.040	0.026	0.012	0.0092
1200	1.0	0.014	0.016	0.043	0.025	0.011	0.0085
1200	0.9	0.014	0.016	0.041	0.025	0.011	0.0084
1200	0.8	0.014	0.015	0.039	0.024	0.011	0.0083
1200	0.7	0.014	0.015	0.038	0.024	0.011	0.0082
1200	0.6	0.013	0.015	0.036	0.023	0.011	0.0081
1200	0.5	0.013	0.015	0.035	0.023	0.011	0.0080
1200	0.4	0.013	0.015	0.035	0.022	0.011	0.0079
1200	0.3	0.013	0.015	0.034	0.022	0.010	0.0078
1200	0.2	0.013	0.014	0.034	0.022	0.010	0.0077
1200	0.1	0.013	0.014	0.033	0.021	0.010	0.0075
1200	0.0	0.013	0.014	0.033	0.021	0.0099	0.0074

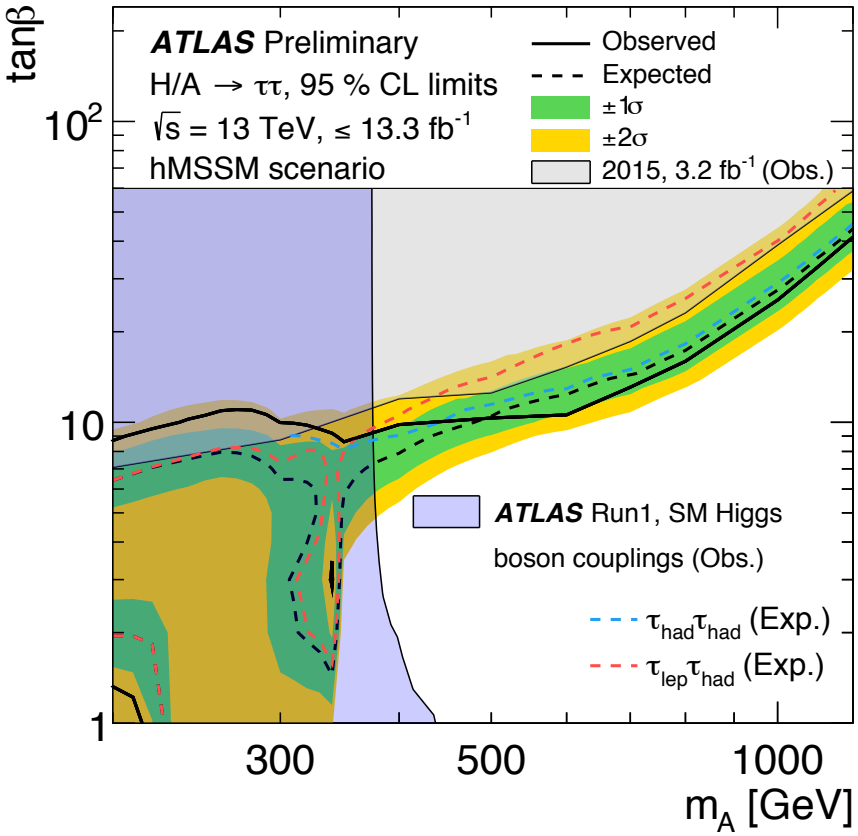

Figure 7: The observed and expected 95% CL limits on $\tan\beta$ as a function of m_A for the combination of $\tau_{\text{lep}}\tau_{\text{had}}$ and $\tau_{\text{had}}\tau_{\text{had}}$ channels in the hMSSM scenario with up to 13.3 fb^{-1} of $\sqrt{s} = 13$ TeV data. Exclusion limits are set also in the low $\tan\beta$ and $m_A = 200$ GeV region and around the mass value $m_A = 350$ GeV. The content is the same as in Figure 5.

References

[1] ATLAS Collaboration, *Observation of a new particle in the search for the Standard Model Higgs boson with the ATLAS detector at the LHC*, Phys. Lett. B **716** (2012) 1, arXiv: 1207.7214 [hep-ex].

[2] CMS Collaboration, *Observation of a new boson at a mass of 125 GeV with the CMS experiment at the LHC*, Phys. Lett. B **716** (2012) 30, arXiv: 1207.7235 [hep-ex].

[3] L. Evans and P. Bryant, *LHC Machine*, JINST **3** (2008) S08001.

[4] ATLAS Collaboration, *Study of the spin and parity of the Higgs boson in diboson decays with the ATLAS detector*, Eur. Phys. J. C **75** (2015) 476, arXiv: 1506.05669 [hep-ex].

[5] ATLAS Collaboration, *Measurements of the Higgs boson production and decay rates and coupling strengths using pp collision data at $\sqrt{s}$ = 7 and 8 TeV in the ATLAS experiment*, Eur. Phys. J. C **76** (2016) 6, arXiv: 1507.04548 [hep-ex].

[6] CMS Collaboration, *Precise determination of the mass of the Higgs boson and tests of compatibility of its couplings with the standard model predictions using proton collisions at 7 and 8 TeV*, Eur. Phys. J. C **75** (2015) 212, arXiv: 1412.8662 [hep-ex].

[7] CMS Collaboration, *Constraints on the spin-parity and anomalous HVV couplings of the Higgs boson in proton collisions at 7 and 8 TeV*, Phys. Rev. D **92** (2015) 012004, arXiv: 1411.3441 [hep-ex].

[8] ATLAS and CMS Collaborations, *Measurements of the Higgs boson production and decay rates and constraints on its couplings from a combined ATLAS and CMS analysis of the LHC pp collision data at $\sqrt{s}$ = 7 and 8 TeV* (2016), arXiv: 1606.02266 [hep-ex].

[9] F. Englert and R. Brout, *Broken symmetry and the mass of gauge vector mesons*, Phys. Rev. Lett. **13** (1964) 321.

[10] P. W. Higgs, *Broken symmetries, massless particles and gauge fields*, Phys. Lett. **12** (1964) 132.

[11] P. W. Higgs, *Broken symmetries and the masses of gauge bosons*, Phys. Rev. Lett. **13** (1964) 508.

[12] P. W. Higgs, *Spontaneous symmetry breakdown without massless bosons*, Phys. Rev. **145** (1966) 1156.

[13] G. Guralnik, C. Hagen and T. Kibble, *Global conservation laws and massless particles*, Phys. Rev. Lett. **13** (1964) 585.

[14] T. Kibble, *Symmetry breaking in non-Abelian gauge theories*, Phys. Rev. **155** (1967) 1554.

[15] A. Djouadi, *The Anatomy of electro-weak symmetry breaking. II. The Higgs bosons in the minimal supersymmetric model*, Phys. Rept. **459** (2008) 1, arXiv: hep-ph/0503173.

[16] G. C. Branco et al., *Theory and phenomenology of two-Higgs-doublet models*, Phys. Rept. **516** (2012) 1, arXiv: 1106.0034 [hep-ph].

[17] P. Fayet, *Supersymmetry and Weak, Electromagnetic and Strong Interactions*, Phys. Lett. B **64** (1976) 159.

[18] P. Fayet, *Spontaneously Broken Supersymmetric Theories of Weak, Electromagnetic and Strong Interactions*, Phys. Lett. B **69** (1977) 489.

[19] M. Carena et al., *MSSM Higgs Boson Searches at the LHC: Benchmark Scenarios after the Discovery of a Higgs-like Particle*, Eur. Phys. J. C **73** (2013) 2552, arXiv: 1302.7033 [hep-ph].

[20] A. Djouadi et al., *The post-Higgs MSSM scenario: Habemus MSSM?*, Eur. Phys. J. C **73** (2013) 2650, arXiv: 1307.5205 [hep-ph].

[21] E. Bagnaschi et al., *Benchmark scenarios for low* tan β *in the MSSM*, LHCHXSWG-2015-002, 2015, URL: http://cdsweb.cern.ch/record/2039911.

[22] ALEPH, DELPHI, L3, and OPAL Collaborations, G. Abbiendi et al., *Search for neutral MSSM Higgs bosons at LEP*, Eur. Phys. J. C **47** (2006) 547, arXiv: hep-ex/0602042 [hep-ex].

[23] Tevatron New Phenomena & Higgs Working Group Collaboration, B. Doug et al., *Combined CDF and D0 upper limits on MSSM Higgs boson production in* $\tau\tau$ *final states with up to* 2.2 fb^{-1} (2010), arXiv: 1003.3363 [hep-ex].

[24] CDF Collaboration, T. Aaltonen et al., *Search for Higgs bosons predicted in two-Higgs-doublet models via decays to* τ *lepton pairs in 1.96 TeV proton–antiproton collisions*, Phys. Rev. Lett. **103** (2009) 201801, arXiv: 0906.1014 [hep-ex].

[25] D0 Collaboration, V. M. Abazov et al., *Search for Higgs bosons decaying to* τ *pairs in* $p\bar{p}$ *collisions with the D0 detector*, Phys. Rev. Lett. **101** (2008) 071804, arXiv: 0805.2491 [hep-ex].

[26] ATLAS Collaboration, *Search for the neutral Higgs bosons of the minimal supersymmetric standard model in pp collisions at* $\sqrt{s} = 7$ *TeV with the ATLAS detector*, JHEP **02** (2013) 095, arXiv: 1211.6956 [hep-ex].

[27] ATLAS Collaboration, *Search for neutral Higgs bosons of the minimal supersymmetric standard model in pp collisions at* $\sqrt{s} = 8$ *TeV with the ATLAS detector*, JHEP **11** (2014) 056, arXiv: 1409.6064 [hep-ex].

[28] CMS Collaboration, *Search for neutral MSSM Higgs bosons decaying to a pair of tau leptons in pp collisions*, JHEP **10** (2014) 160, arXiv: 1408.3316 [hep-ex].

[29] CMS Collaboration, *Search for Neutral MSSM Higgs Bosons Decaying into A Pair of Bottom Quarks*, JHEP **11** (2015) 071, arXiv: 1506.08329 [hep-ex].

[30] LHCb Collaboration, R. Aaij et al., *Limits on neutral Higgs boson production in the forward region in pp collisions at* $\sqrt{s} = 7$ *TeV*, JHEP **05** (2013) 132, arXiv: 1304.2591 [hep-ex].

[31] ATLAS Collaboration, *Search for Minimal Supersymmetric Standard Model Higgs bosons* H/A *and for a* Z' *boson in the* $\tau\tau$ *final state produced in pp collisions at* $\sqrt{s} = 13$ TeV *with the ATLAS Detector* (2016), arXiv: 1608.00890 [hep-ex].

[32] CMS Collaboration, *Search for a neutral MSSM Higgs boson decaying into* $\tau\tau$ *at 13 TeV*, CMS-PAS-HIG-16-006, 2016, URL: http://cds.cern.ch/record/2160252.

[33] ATLAS Collaboration, *The ATLAS experiment at the CERN Large Hadron Collider*, JINST **3** (2008) S08003.

[34] ATLAS Collaboration, *ATLAS Insertable B-Layer Technical Design Report*, ATLAS-TDR-19, 2010, URL: http://cds.cern.ch/record/1291633,
ATLAS Insertable B-Layer Technical Design Report Addendum, ATLAS-TDR-19-ADD-1, 2012, URL: http://cds.cern.ch/record/1451888.

[35] ATLAS Collaboration, *Improved luminosity determination in pp collisions at $\sqrt{s}$ = 7 TeV using the ATLAS detector at the LHC*, Eur. Phys. J. C **73** (2013) 2518, arXiv: 1302.4393 [hep-ex].

[36] P. Nason, *A New method for combining NLO QCD with shower Monte Carlo algorithms*, JHEP **11** (2004) 040, arXiv: hep-ph/0409146.

[37] S. Frixione, P. Nason and C. Oleari,
Matching NLO QCD computations with Parton Shower simulations: the POWHEG method, JHEP **11** (2007) 070, arXiv: 0709.2092 [hep-ph].

[38] S. Alioli et al., *A general framework for implementing NLO calculations in shower Monte Carlo programs: the POWHEG BOX*, JHEP **06** (2010) 043, arXiv: 1002.2581 [hep-ph].

[39] J. Alwall et al., *The automated computation of tree-level and next-to-leading order differential cross sections, and their matching to parton shower simulations*, JHEP **07** (2014) 079, arXiv: 1405.0301 [hep-ph].

[40] M. Wiesemann et al., *Higgs production in association with bottom quarks*, JHEP **02** (2015) 132, arXiv: 1409.5301 [hep-ph].

[41] H.-L. Lai et al., *New parton distributions for collider physics*, Phys. Rev. D **82** (2010) 074024, arXiv: 1007.2241 [hep-ph].

[42] S. Dulat et al.,
New parton distribution functions from a global analysis of quantum chromodynamics, Phys. Rev. D **93** (2016) 033006, arXiv: 1506.07443 [hep-ph].

[43] T. Sjöstrand et al., *An Introduction to PYTHIA 8.2*, Comput. Phys. Commun. **191** (2015) 159, arXiv: 1410.3012 [hep-ph].

[44] ATLAS Collaboration, *Measurement of the Z/γ^* boson transverse momentum distribution in pp collisions at $\sqrt{s}$ = 7 TeV with the ATLAS detector*, JHEP **09** (2014) 55, arXiv: 1406.3660 [hep-ex].

[45] ATLAS Collaboration, *ATLAS Run 1 Pythia8 tunes*, ATL-PHYS-PUB-2014-021, 2014, URL: http://cdsweb.cern.ch/record/1966419.

[46] R. V. Harlander, S. Liebler and H. Mantler, *SusHi: A program for the calculation of Higgs production in gluon fusion and bottom-quark annihilation in the Standard Model and the MSSM*, Comp. Phys. Commun. **184** (2013) 1605, arXiv: 1212.3249 [hep-ph].

[47] R. V. Harlander and W. B. Kilgore,
Next-to-Next-to-Leading Order Higgs Production at Hadron Colliders, Phys. Rev. Lett. **88** (2002) 201801, arXiv: hep-ph/0201206.

[48] M. Spira et al., *Higgs boson production at the LHC*, Nucl. Phys. B **453** (1995) 17, arXiv: hep-ph/9504378.

[49] C. Anastasiou and K. Melnikov, *Higgs boson production at hadron colliders in NNLO QCD*, Nucl. Phys. B **646** (2002) 220, arXiv: hep-ph/0207004.

[50] V. Ravindran, J. Smith and W. L. van Neerven, *NNLO corrections to the total cross-section for Higgs boson production in hadron hadron collisions*, Nucl. Phys. B **665** (2003) 325, arXiv: hep-ph/0302135.

[51] R. Harlander and W. B. Kilgore, *Production of a pseudoscalar Higgs boson at hadron colliders at next-to-next-to leading order*, JHEP **10** (2002) 017, arXiv: hep-ph/0208096.

[52] C. Anastasiou and K. Melnikov, *Pseudoscalar Higgs boson production at hadron colliders in NNLO QCD*, Phys. Rev. D **67** (2003) 037501, arXiv: hep-ph/0208115.

[53] U. Aglietti et al., *Two loop light fermion contribution to Higgs production and decays*, Phys. Lett. B **595** (2004) 432, arXiv: hep-ph/0404071.

[54] R. Bonciani, G. Degrassi and A. Vicini, *On the Generalized Harmonic Polylogarithms of One Complex Variable*, Comput. Phys. Commun. **182** (2011) 1253, arXiv: 1007.1891 [hep-ph].

[55] R. V. Harlander and M. Steinhauser, *Supersymmetric Higgs production in gluon fusion at next-to-leading order*, JHEP **09** (2004) 066, arXiv: hep-ph/0409010.

[56] R. Harlander and P. Kant, *Higgs production and decay: Analytic results at next-to-leading order QCD*, JHEP **12** (2005) 015, arXiv: hep-ph/0509189.

[57] G. Degrassi and P. Slavich, *NLO QCD bottom corrections to Higgs boson production in the MSSM*, JHEP **11** (2010) 044, arXiv: 1007.3465 [hep-ph].

[58] G. Degrassi, S. Di Vita and P. Slavich, *NLO QCD corrections to pseudoscalar Higgs production in the MSSM*, JHEP **08** (2011) 128, arXiv: 1107.0914 [hep-ph].

[59] G. Degrassi, S. Di Vita and P. Slavich, *On the NLO QCD Corrections to the Production of the Heaviest Neutral Higgs Scalar in the MSSM*, Eur. Phys. J. C **72** (2012) 2032, arXiv: 1204.1016 [hep-ph].

[60] R. Harlander and W. B. Kilgore, *Higgs boson production in bottom quark fusion at next-to-next-to-leading order*, Phys. Rev. D **68** (2003) 013001, arXiv: hep-ph/0304035.

[61] S. Dittmaier, M. Krämer and M. Spira, *Higgs radiation off bottom quarks at the Tevatron and the LHC*, Phys. Rev. D **70** (2004) 074010, arXiv: hep-ph/0309204.

[62] S. Dawson, C. B. Jackson, L. Reina and D. Wackeroth, *Exclusive Higgs boson production with bottom quarks at hadron colliders*, Phys. Rev. D **69** (2004) 074027, arXiv: hep-ph/0311067.

[63] R. Harlander, M. Krämer and M. Schumacher, *Bottom-quark associated Higgs-boson production: reconciling the four- and five-flavour scheme approach* (2011), arXiv: 1112.3478 [hep-ph].

[64] S. Heinemeyer, W. Hollik and G. Weiglein, *FeynHiggs: A Program for the calculation of the masses of the neutral CP even Higgs bosons in the MSSM*, Comput. Phys. Commun. **124** (2000) 76, arXiv: hep-ph/9812320.

[65] S. Heinemeyer, W. Hollik and G. Weiglein, *The Masses of the neutral CP - even Higgs bosons in the MSSM: Accurate analysis at the two loop level*, Eur. Phys. J. C **9** (1999) 343, arXiv: hep-ph/9812472.

[66] M. Frank et al., *The Higgs Boson Masses and Mixings of the Complex MSSM in the Feynman-Diagrammatic Approach*, JHEP **02** (2007) 047, arXiv: hep-ph/0611326.

[67] G. Degrassi et al., *Towards high precision predictions for the MSSM Higgs sector*, Eur. Phys. J. C **28** (2003) 133, arXiv: hep-ph/0212020.

[68] T. Hahn et al., *High-Precision Predictions for the Light CP -Even Higgs Boson Mass of the Minimal Supersymmetric Standard Model*, Phys. Rev. Lett. **112** (2014) 141801, arXiv: 1312.4937 [hep-ph].

[69] LHC Higgs Cross Section Working Group, *Handbook of LHC Higgs Cross Sections: 3. Higgs Properties*, CERN-2013-004 (CERN, Geneva, 2013), arXiv: 1307.1347 [hep-ph].

[70] A. Djouadi, J. Kalinowski and M. Spira, *HDECAY: A Program for Higgs boson decays in the standard model and its supersymmetric extension*, Comput. Phys. Commun. **108** (1998) 56, arXiv: hep-ph/9704448.

[71] E. Barberio, B. V. Eijk and Z. Was, *PHOTOS - a universal Monte Carlo for QED radiative corrections in decays*, Comput. Phys. Commun. **66** (1991) 115.

[72] N. Davidson, T. Przedzinski and Z. Was, *PHOTOS Interface in C++: Technical and Physics Documentation*, Comput. Phys. Commun. **199** (2016) 86, arXiv: 1011.0937 [hep-ph].

[73] T. Gleisberg et al., *Event generation with SHERPA 1.1*, JHEP **02** (2009) 007, arXiv: 0811.4622 [hep-ph].

[74] S. Höche et al., *QCD matrix elements + parton showers: The NLO case*, JHEP **04** (2013) 027, arXiv: 1207.5030 [hep-ph].

[75] C. Anastasiou et al., *High precision QCD at hadron colliders: Electroweak gauge boson rapidity distributions at NNLO*, Phys. Rev. D **69** (2004) 094008, arXiv: hep-ph/0312266.

[76] K. Melnikov and F. Petriello, *Electroweak gauge boson production at hadron colliders through O(alpha(s)**2)*, Phys. Rev. D **74** (2006) 114017, arXiv: hep-ph/0609070.

[77] R. Gavin et al., *FEWZ 2.0: A code for hadronic Z production at next-to-next-to-leading order*, Comput. Phys. Commun. **182** (2011) 2388, arXiv: 1011.3540 [hep-ph].

[78] P. Artoisenet et al., *Automatic spin-entangled decays of heavy resonances in Monte Carlo simulations*, JHEP **03** (2013) 015, arXiv: 1212.3460 [hep-ph].

[79] T. Sjöstrand, S. Mrenna and P. Skands, *PYTHIA 6.4 physics and manual*, JHEP **05** (2006) 026, arXiv: hep-ph/0603175.

[80] P. Skands, *Tuning Monte Carlo Generators: The Perugia Tunes*, Phys. Rev. D **82** (2010) 074018, arXiv: 1005.3457 [hep-ph].

[81] M. Czakon and A. Mitov, *Top++: A Program for the Calculation of the Top-Pair Cross-Section at Hadron Colliders*, Comput. Phys. Commun. **185** (2014) 2930, arXiv: 1112.5675 [hep-ph].

[82] N. Kidonakis, *Next-to-next-to-leading-order collinear and soft gluon corrections for t-channel single top quark production*, Phys. Rev. D **83** (2011) 091503, arXiv: 1103.2792 [hep-ph].

[83] N. Kidonakis, *NNLL resummation for s-channel single top quark production*, Phys. Rev. D **81** (2010) 054028, arXiv: 1001.5034 [hep-ph].

[84] N. Kidonakis, *Two-loop soft anomalous dimensions for single top quark associated production with a W- or H-*, Phys. Rev. D **82** (2010) 054018, arXiv: 1005.4451 [hep-ph].

[85] D. J. Lange, *The EvtGen particle decay simulation package*, Nucl. Instrum. Meth. A **462** (2001) 152.

[86] T. Sjöstrand, S. Mrenna and P. Skands, *A Brief Introduction to PYTHIA 8.1*, Comput. Phys. Commun. **178** (2008) 852, arXiv: 0710.3820 [hep-ph].

[87] ATLAS Collaboration, *Summary of ATLAS Pythia 8 tunes*, ATL-PHYS-PUB-2012-003, 2012, URL: http://cdsweb.cern.ch/record/1474107.

[88] A. D. Martin et al., *Parton distributions for the LHC*, Eur. Phys. J. C **63** (2009) 189, arXiv: 0901.0002 [hep-ph].

[89] ATLAS Collaboration, *The ATLAS simulation infrastructure*, Eur. Phys. J. C **70** (2010) 823, arXiv: 1005.4568 [physics.ins-det].

[90] S. Agostinelli et al., GEANT4 Collaboration, *GEANT4 - a simulation toolkit*, Nucl. Instrum. Meth. A **506** (2003) 250.

[91] ATLAS Collaboration, *The simulation principle and performance of the ATLAS fast calorimeter simulation FastCaloSim*, ATL-PHYS-PUB-2010-013, 2010, URL: http://cdsweb.cern.ch/record/1300517.

[92] ATLAS Collaboration, *Electron and photon energy calibration with the ATLAS detector using LHC Run 1 data*, Eur. Phys. J. C **74** (2014) 3071, arXiv: 1407.5063 [hep-ex].

[93] ATLAS Collaboration, *Electron efficiency measurements with the ATLAS detector using the 2015 LHC proton-proton collision data*, ATLAS-CONF-2016-024, 2016, URL: http://cdsweb.cern.ch/record/2157687.

[94] ATLAS Collaboration, *Muon reconstruction performance of the ATLAS detector in proton–proton collision data at* $\sqrt{s}$*=13 TeV*, Eur. Phys. J. C **76** (2016) 292, arXiv: 1603.05598 [hep-ex].

[95] ATLAS Collaboration, *Topological cell clustering in the ATLAS calorimeters and its performance in LHC Run 1* (2016), arXiv: 1603.02934 [hep-ex].

[96] M. Cacciari, G. P. Salam and G. Soyez, *The anti-*k_t *jet clustering algorithm*, JHEP **04** (2008) 063, arXiv: 0802.1189 [hep-ph].

[97] ATLAS Collaboration, *Tagging and suppression of pileup jets with the ATLAS detector*, ATLAS-CONF-2014-018, 2014, URL: http://cdsweb.cern.ch/record/1700870.

[98] ATLAS Collaboration, *Expected performance of the ATLAS b-tagging algorithms in Run-2*, ATL-PHYS-PUB-2015-022, 2015, URL: http://cdsweb.cern.ch/record/2037697.

[99] ATLAS Collaboration, *Commissioning of the ATLAS b-tagging algorithms using $t\bar{t}$ events in early Run-2 data*, ATL-PHYS-PUB-2015-039, 2015, URL: http://cdsweb.cern.ch/record/2047871.

[100] ATLAS Collaboration, *Reconstruction, Energy Calibration, and Identification of Hadronically Decaying Tau Leptons in the ATLAS Experiment for Run-2 of the LHC*, ATL-PHYS-PUB-2015-045, 2015, URL: http://cdsweb.cern.ch/record/2064383.

[101] ATLAS Collaboration, *Performance of missing transverse momentum reconstruction for the ATLAS detector in the first proton-proton collisions at $\sqrt{s}$= 13 TeV*, ATL-PHYS-PUB-2015-027, 2015, URL: http://cdsweb.cern.ch/record/2037904.

[102] M. Aliev et al., *HATHOR: HAdronic Top and Heavy quarks crOss section calculatoR*, Comput. Phys. Commun. **182** (2011) 1034, arXiv: 1007.1327 [hep-ph].

[103] P. Kant et al., *HATHOR for single top-quark production: Updated predictions and uncertainty estimates for single top-quark production in hadronic collisions*, Comput. Phys. Commun. **191** (2015) 74, arXiv: 1406.4403 [hep-ph].

[104] ATLAS Collaboration, *Simulation of top-quark production for the ATLAS experiment at $\sqrt{s}$ = 13 TeV*, ATL-PHYS-PUB-2016-004, 2016, URL: http://cdsweb.cern.ch/record/2120417.

[105] M. Bahr et al., *Herwig++ Physics and Manual*, Eur. Phys. J. C **58** (2008) 639, arXiv: 0803.0883 [hep-ph].

[106] R. D. Ball et al., *Parton distributions for the LHC Run II*, JHEP **04** (2015) 040, arXiv: 1410.8849 [hep-ph].

[107] A. Martin et al., *Heavy-quark mass dependence in global PDF analyses and 3- and 4-flavour parton distributions*, Eur. Phys. J. C **70** (2010) 51, arXiv: 1007.2624 [hep-ph].

[108] G. Cowan et al., *Asymptotic formulae for likelihood-based tests of new physics*, Eur. Phys. J. C **71** (2011) 1554, [Erratum: Eur. Phys. J. C 73 (2013) 2501], arXiv: 1007.1727 [physics.data-an].

[109] A. L. Read, *Presentation of search results: the CL_s technique*, J. Phys. G **28** (2002) 2693.

[110] ATLAS Collaboration, *Constraints on new phenomena via Higgs boson couplings and invisible decays with the ATLAS detector*, JHEP **11** (2015) 206, arXiv: 1509.00672 [hep-ex].